Nanocarbon-based electrochemical systems for sensing, electrocatalysis, and energy storage

Citation: Mao, Xianwen, Gregory C. Rutledge, and T. Alan Hatton. "Nanocarbon-based electrochemical systems for sensing, electrocatalysis, and energy storage." Nanotoday 9:4 (August 2014), pp. 405-432.

As Published: http://dx.doi.org/10.1016/j.nantod.2014.06.011

Publisher: Elsevier

Persistent URL: http://hdl.handle.net/1721.1/104062

Version: Author's final manuscript: final author's manuscript post peer review, without publisher's formatting or copy editing

Carbon Nanofiber-, Carbon Nanotube- and Graphene-Based Electrochemical Systems for Sensing, Electrocatalysis, and Energy Storage

*Xianwen Mao, Gregory C. Rutledge, and T. Alan Hatton**

Department of Chemical Engineering, Massachusetts Institute of Technology, 77 Massachusetts Avenue, Cambridge, Massachusetts, 02139, USA

* Corresponding author: tahatton@mit.edu,

Keywords: carbon nanofiber; carbon nanotube; graphene; electrochemistry; sensing; electrocatalysis; energy storage;

Introduction

Carbon materials are used extensively in both analytical and industrial electrochemistry, and are important for many electrochemical applications due to their tunable electron-transfer and charge-storage properties.[1, 2] Carbon has several advantages relative to other electrode materials, including low cost, a wide working window (i.e., the electrochemical potential range over which the electrode can perform its normal function), and high electrocatalytic activities for a variety of redox-active chemical and biological systems. Structural manipulation of carbon to modulate its chemical, electronic, and crystalline properties is key to the design of many high-performance electrochemical devices, for example, sensors,[3] lithium-ion batteries,[4] and supercapacitors,[5] to name a few. Moreover, carbon surfaces can be modified easily by a variety of noncovalent and covalent methods, thereby broadening significantly the utility of carbon electrodes. Noncovalent modification mostly relies on π-stacking interactions between the adsorbates and carbon surfaces. Common chemical structures that exhibit π-stacking interactions with sp^2-conjugated carbon surfaces include nucleotide bases,[6-9] pyrenes,[10-12] porphyrins,[13-15] and metallocenes.[16, 17] Various types of reactions have been exploited to modify carbon surfaces covalently; most commonly used reactions are diazonium ion reduction,[18] amine oxidation,[19] photochemical reactions,[20] and click cycloaddition chemistry.[21]

Here we focus on three types of carbon nanomaterials of recent interest in electrochemistry, namely, carbon nanofibers (CNFs), carbon nanotubes (CNTs), and graphene. Electrochemical applications of the "classical" carbon materials based upon graphite, glassy carbon, and carbon black have been covered extensively in several earlier reviews and monographs.[22][23][24] In this review, following a brief overview of the synthesis methods for each class of carbon nanomaterials, we discuss their electrochemical applications for sensing, electrocatalysis, and energy storage (including both supercapacitor and lithium ion battery (LIB) applications). The field of nanocarbon electrochemistry has developed rapidly in recent years; this review focuses primarily on general strategies developed for the manipulation of carbon structure, as summarized in **Table 1**, with emphasis on elucidation of the

relevant structure-property relationships for each application area for carbon nanofibers, nanotubes, and graphene. We devote special attention to the intrinsic properties of carbon nanomaterials that give rise to their high electrochemical activities; hence, in the last section of this review we discuss how the electronic structure of carbon influences its performance for sensing, catalysis and energy storage.

Synthesis of CNFs, CNTs and Graphene-Based Materials

Fibrous carbon materials have attracted widespread attention, both fundamentally and for practical applications.[25] In the late 1950s, Bacon succeeded in producing the first high performance carbon fibers.[25] A few years later, in the early1960s, polyacrylonitrile (PAN)-based carbon fibers were developed by Shindo,[26] following which Singer, in 1970, developed pitch-based carbon fibers.[27] Generally, carbon fibers are produced either by pyrolyzing fibers spun from an organic precursor, or by chemical vapor deposition (CVD).[28] The major spinnable carbon precursors include PAN, pitch, polybenzimidazol (PBI), poly(amic acid) (PAA), phenolic resin, polyvinylpyrrolidone (PVP), polyimide (PI), poly(vinyl alcohol) (PVA), and cellulose acetate (CA).[29, 30] Recently, electrospinning followed by thermal treatment has emerged as a simple, efficient and scalable method to generate ultrafine carbon nanofibers.[30] Electrospinning has the advantages of simplicity, efficiency, low cost, high yield and high degree of reproducibility of the obtained materials. The versatility of electrospinning is not only related to the nature of the precursors and electrospun materials, but also extends to the fiber assemblies and architectures of the final products. Modifications of solution and processing parameters[31, 32] and/or set-up geometries[33] permit the preparation of complex nanostructures with controllable hierarchical features such as nonwoven, aligned or patterned fibers, nanoribbons, nanorods, random three dimensional structures, sub-micron springs and convoluted fibers with controlled diameters. Additionally, the possibility of co-electrospinning different solutions using specially designed spinnerets leads to the elaboration of core–sheath fibers,[33, 34] hollow fibers,[35] porous fibers,[36] and multichannel tubes.[37]

Carbon is well known to form distinct solid state allotropes with diverse structures and properties. CNTs can be viewed as one-dimensional cylinders composed of a single layer or a few layers of graphene with high length-to-diameter ratios ranging from 10^2 to 10^7. The first observations of CNTs and their subsequent large-scale synthesis using arc discharge techniques were reported by Iijima and coworkers.[38] Laser ablation was later demonstrated by Smalley et al.[39] to be an alternative method for growing CNTs. Once it was observed that transition metals embedded in graphite electrodes produced carbon nanotubes with higher yield and reproducibility,[40] chemical vapor deposition using transition metal nanoparticle catalysts was developed to produce high quality single-walled and multi-walled CNTs (SWCNTs and MWCNTs, respectively) in vertically aligned arrays.[41, 42] Vertically aligned arrays can also be grown on metallic and quasicrystalline substrates. The metal nanoparticle catalyst concept was extended later to the synthesis of CNTs by pyrolysis of metal carbonyls in the presence of other hydrocarbons.[43] When optimized in a high pressure carbon monoxide (HiPco) environment, the carbonyl pyrolysis process led to high yield production of SWCNTs.[44]

Graphene is the latest carbon nanomaterial to be isolated; this feat was accomplished on an insulating substrate and the allotrope was electrically characterized by Novoselov et al. in 2004.[45] Graphene is often viewed as

the two-dimensional building block for other sp^2 hybridized carbon nanomaterials because, conceptually, it can be rolled or distorted to form carbon nanotubes and fullerenes. In 1962, Boehm et al.[46] reported the existence of very thin carbon foils, produced from the reduction of graphite oxide in a dilute alkaline solution. In 1998, Forbeaux et al.[47] reported a heteroepitaxial growth method that opens up the possibility for isolation of a single graphene layer above a substrate. In addition, some attempts at mechanical isolation of graphene were made prior to 2004.[48] However, the most definitive evidence of monolayer graphene and its electrical properties was provided by the Manchester group using mechanically exfoliated graphene.[45] Although historically significant, this so-called "Scotch tape" technique for producing graphene lacks sufficient scalability for most applications. To address this issue, epitaxial graphene has been realized by graphitization of both doped and undoped silicon carbide (SiC) single crystal wafers at high temperatures.[49] Claims of epitaxial monolayer graphite (MG) on metal carbides at high temperatures using hydrocarbon precursors also exist from the early 1990's as has been comprehensively reviewed elsewhere.[50] Nevertheless, only the recent work on SiC has demonstrated graphene growth with sufficient quality for electronic applications. While this approach to epitaxial graphene offers wafer-scale growth, it is difficult to achieve uniform monolayer graphene coverage, and the product suffers from inferior electronic properties compared to mechanically exfoliated graphene.[49]

Solution-processing is another important technique to synthesize graphene at low cost in a scalable manner. The earliest reports of 'graphite oxide' synthesis trace back to the work of Hummers.[51] Similar methods were employed by the Ruoff group in 2006 to create graphene oxide (GO) that was mostly single layered.[52, 53] All of these methods result in an aqueous dispersion/colloid of thin GO flakes, obtained by subjecting graphite to highly oxidizing conditions that allows functionalization of the basal plane of graphene with hydrophilic functional groups.[35,36] The resulting GO can be reduced partially to form reduced graphene oxide (rGO) *via* chemical methods,[54] and by annealing in reducing environments.[55] A few variants of these oxidation and reduction processes have been developed and are summarized in recent reviews.[56, 57] Although this method is promising for large-scale solution processing of graphene-based materials, the harsh oxidizing conditions can damage the basal plane of grapheme irreversibly, leading to deterioration of its properties. This problem can be circumvented partially by direct exfoliation of graphene from graphite using ultrasonication with suitable choice of surfactants and solvents.[58, 59] In all cases, solution-based methods for preparing single-layer graphene result in relatively small flakes that are sub-optimal for wafer-scale applications. CVD growth on metallic substrates such as nickel and copper, however, provides a pathway to making large-area graphene sheets.[60-63] CVD-grown graphene is continuous with uniform thickness over large areas, thus making it promising for electronic applications. CVD graphene on copper/nickel and solution-processed graphene are currently produced in bulk quantities and are commercially available.

Electrochemical Sensing

Electrospun CNFs are attractive for electrochemical sensing because their electrochemical activities can be adjusted easily through the tailoring of processing conditions (e.g., composition of the precursor solution and thermal treatment conditions). Incorporation of metal nanoparticles into electrospun CNFs can be accomplished

readily by mixing metal salts with precursor solutions. This strategy is useful for generating metal/CNF composites with remarkably enhanced sensing performance. Examples of carbon nanomaterials used in the development of electrochemical sensors are shown in **Figures 1**. Huang et al.[64] synthesized palladium nanoparticle-loaded electrospun CNFs (Pd/CNFs) in which the spherical Pd nanoparticles were well-dispersed on the surfaces of CNFs or embedded within them (**Figure 1a**). X-ray diffraction (XRD) measurements (**Figure 1b**) confirmed the presence of both Pd nanoparticles and graphitic carbon. The cubic phase of Pd was formed during the carbonization process, and the presence of Pd nanoparticles also promoted the carbonization of the precursor polymer fibers. The Pd/CNF-modified carbon paste electrode (CPE) demonstrated direct responses to H_2O_2 and NADH at low potentials, without any enzymatic mediation. **Figure 1c** shows the current response of a Pd/CNF modified CPE electrode upon successive addition of H_2O_2; significant changes in the magnitude of the observed electric current upon addition of hydrogen peroxide indicate the ability of the electrode to detect this molecule. A linear relationship between the current and the H_2O_2 concentration ranging from 0.2 μM to 20 mM was observed. Researchers from the same group also reported the synthesis of platinum nanoparticle-laden CNFs for H_2O_2 detection.[65] Another research group[66] used a similar electrospinning/thermal treatment approach to fabricate rhodium nanoparticle-loaded CNFs. These authors showed that the hybrid system exhibits high electrocatalytic activity for hydrazine oxidation and, potentially, can be used for the amperometric sensing of hydrazine with high sensitivity and good selectivity.

Mao et al.[3] employed a different route to manipulate the electrochemical activities of electrospun CNFs. Instead of using additional active components, these authors focused on modulating the intrinsic electronic properties of CNFs themselves. They found that by adjusting the densities of states (DOS) of electrospun CNF webs they were able to modulate the electron transfer kinetics and efficiencies of the CNFs towards various chemical and biological systems. This strategy to control electron transfer processes can apply to different types of redox species; such general strategies are unusual since the electron transfer behaviors of different redox species are usually affected by a variety of factors such as oxygen-containing functional groups, carbon edge sites, and complicated surface characteristics that govern the adsorption force between the analyte and the electrode.[1] Furthermore, continuous all-carbon CNFs with high DOS can be deposited directly onto substrates via an electrospinning-based process for the development of electrochemical sensors with ultra-wide dynamic ranges and high sensitivities.[67] Also, direct electron transfer (DET) with many redox enzymes strongly depends on the DOS of the supporting electrode.[68] Therefore, development of methods for the control of DOS in electrodes can be advantageous in that they allow modulation of the DET efficiencies with enzymes for many applications, such as highly selective biosensors,[69] bioelectronics,[70] enzyme catalysts,[71] and biofuel cells.[72-74]

Recently CNTs and graphene have been used increasingly for electrochemical sensing of redox-active species (e.g., dopamine, DA). These two carbon allotropes offer unique electron transport properties. Generally SWCNTs are a mixture of metallic and semiconducting species, depending sensitively on their geometrical characteristics, while MWCNTs are regarded as metallic conductors. Additionally, as a result of their one dimensional nature, CNTs can conduct electrons without energy dissipation as heat (i.e., ballistic transport). Graphene is intrinsically a semi-metal or zero-gap semiconductor; the electrons and holes in graphene behave as if they have no

mass, and their density of electronic states depends linearly on energy.[75] A more detailed discussion on the electronic structure of graphene is provided later. For electrochemical sensing applications, CNT- or graphene-based sensors generally have higher sensitivities, lower limits of detection, and faster electron transfer kinetics than do traditional carbon electrodes such as CPE.

The first paper to report on the use of CNTs in the study of dopamine detection was published in 1996 by Britto et al.[76] They mixed MWCNTs with bromoform to form a paste that was then packed into a glass tube to prepare a CPE. A regular CPE and a CNT-CPE were compared by studying the oxidation of dopamine by cyclic voltammetry and differential pulse voltammetry. The CNT-CPE showed increased sensitivity for dopamine and nearly ideal, reversible kinetics, which is unusual for dopamine at carbon electrodes.[1] CNTs can also be grown on different substrates and then used directly as electrodes. Macpherson's group grew ultrathin CNT mats (**Figure 1d**) on insulating Si surfaces by CVD.[77] For electrochemical evaluation, a 100 μm ultramicroelectrode (UME) was fabricated using lithography, with the CNT mat as the electrode material. A schematic of the device used is shown in **Figure 1e**. The CNT networks retained a low capacitance and background signal, and exhibited efficient transfer with dopamine over multiple scans. **Figure 1f** shows the cyclic voltammograms (CVs) recorded by the device for the oxidation of DA; there was a good scaling of the limiting current with DA concentration, down to 1 μM (Figure 1e inset). CV measurements were also performed under conditions that mimic an in vivo environment, i.e., 4% albumin in phosphate buffer solution (PBS) w/w (**Figure 1g**). A perfect scaling between the limiting current and the DA concentration was also observed (**Figure 1g inset**). The slight decrease in limiting current when the background electrolyte was changed from PBS to albumin was attributed to a decrease in the diffusion coefficient of DA in the more viscous albumin medium.

Shang et al.[78] were the first researchers to use graphene-based nanomaterials for electrochemical sensing. They grew multilayer graphene nanoflake films (MGNFs) (**Figure 1h, 1i**) on silica substrates using a catalyst-free method. MGNFs have a typical thickness of several tens of nanometers and thus contain several hundred stacked graphene sheets. The MGNF electrode demonstrated good performance for detection of DA in the presence of ascorbic acid (AA), and uric acid (UA) (**Figure 1j, 1k**). The electrochemical performance of the MGNF electrode was superior to that of a glassy-carbon electrode (GCE) but comparable to that of an edge-plane pyrolytic graphite (EPPG) electrode.

Common modification techniques for CNTs to improve their electrochemical sensing performance (i.e., enhancing sensitivity and selectivity) include functionalization with conducting polymers,[79-81] mixing with surfactants or polyelectrolytes,[82-84] modification with metal oxides or nanoparticles,[85-88] incorporation of enzymes[84, 89, 90] and doping with heteroatoms.[91, 92] In addition, field effect transistors composed of aligned carbon nanotubes with proper surface modifications can also be used as chemical or electrochemical sensors.[93, 94]

Li et al. modified a GCE by electro-copolymerizing overoxidized polypyrrole (OPPY) and SWCNT onto the surface.[80] The selectivity of the electrode was tested by investigating the redox reactions of $Fe(CN)_6^{3-}$ and $Ru(NH_3)_6^{3+}$; the electrode exhibited cationic selectivity. The OPPY films were permeable to cations such as dopamine, but the films repelled anions and neutral compounds, such as ascorbic acid and serotonin.[79] In a similar study, MWCNT and OPPY were electro-copolymerized onto a GCE.[81] The OPPY–MWCNT-modified GCE had

an increased sensitivity to dopamine, but in experiments to investigate selectivity with $Fe(CN)_6^{3-}$ and $Ru(NH_3)_6^{3+}$, $Fe(CN)_6^{3-}$ detection was significantly, but not completely, inhibited.

Zheng et al. grew MWCNTs on a Ta substrate and then functionalized them with sodium dodecyl sulfate (SDS) to detect dopamine in the presence of ascorbic acid.[82] In their differential pulse voltammetry (DPV) studies, they obtained a limit of detection (LOD) of 3.75 μM for dopamine in the presence of ascorbic acid ranging from 0.02 mM to 0.2 mM. However, this method was not sensitive enough to detect dopamine in real biological samples, where levels are in the nM range.

Jiang et al. found that modification of a MWCNT forest electrode with RuO_2 resulted in a larger signal than when they used just MWCNTs on their own.[85] Ascorbic acid, uric acid, and dopamine could be discriminated using DPV. A 60 nM LOD was estimated, although only much higher concentrations, in the μM to mM range, were actually tested in the study.

Han et al.[86] prepared MWCNT-grafted poly(lactic acid) (MWCNT-g-PLA) by intercalative polymerization of poly(lactic acid) in the presence of MWCNTs functionalized with hydroxyl groups. Pd nanoparticles were then crystallized on the surfaces of the MWCNT-g-PLA clusters. The resulting Pd-loaded sensing system exhibited a significantly lower LOD for hydrogen peroxide than did MWCNT-g-PLA without Pd nanoparticles. This system also provided good stability and selectivity towards interferences such as UA, AA, and glucose.

Butwong et al.[87] utilized electrochemical deposition to modify MWCNTs with cadmium oxide (CdO) nanoparticles ~ 50 nm in diameter. The resulting CdO/MWCNT sensor displayed a high synergistic electrocatalytic activity towards detection of H_2O_2, with a much lower detection limit than shown by the two individual components alone. The sensor was able to reduce H_2O_2 at −1.2 V versus Ag/AgCl over a broad pH range. At the optimal pH of 7, the sensor exhibited a detection limit of 0.1 μM, a dynamic range from 0.5 to 200 μM, good reproducibility, and long-term stability. Uric acid, ascorbic acid and dopamine up to 100 μM provoked no signal response, attesting to the selectivity of the CdO/MWCNT modified electrode for hydrogen peroxide.

In other work by Gao et al.,[88] a nonenzymatic sensor based on $Ni(OH)_2$ nanoparticles, electroreduced graphene oxide (ERGO), and MWCNTs was fabricated via convenient electrodeposition of $Ni(OH)_2$ nanoparticles on ERGO-MWCNT film modified glass carbon electrodes. Graphene oxide sheets served as surfactants to stabilize the dispersion of pristine MWCNTs in aqueous solution, rendering a fine coverage of ERGO-MWNT film on the glass carbon electrode during the fabrication process. MWCNTs functioned as conducting bridges between the ERGO sheets to enhance the electron transfer rate. When the advantages of ERGO and MWNTs were combined in this way, together with the electrocatalytic effect of $Ni(OH)_2$ nanoparticles, the hybrid sensor exhibited excellent sensing behavior towards glucose and hydrogen peroxide. The dynamic ranges for detection of glucose and H_2O_2 were 10 – 1500 μM and 10 – 9050 μM, respectively, with respective detection limits of 2.7 μM and 4.0 μM. These results indicate that $Ni(OH)_2$/ERGO-MWCNT hybrids are promising electrode materials for biosensing. Additionally, good recoveries of analytes in real samples such as urine and milk confirmed the reliability of the prepared sensor for practical applications.

A novel study proposed utilizing the enzyme laccase to determine dopamine selectively in the presence of ascorbic acid and DOPAC (3,4-dihydroxyphenylacetic acid), a metabolite of dopamine.[89] Laccase catalyzes the

oxidization of dopamine to dopamine-o-quinone, which can cyclize and be oxidized by laccase again to form 5,6-dihydroxyindoline quinone. The 5,6-dihydroxyindoline quinone has a reduction peak at a negative potential that is completely separate from those of ascorbic acid and DOPAC. Detection by a reduction peak is advantageous because most existing methods detect dopamine oxidation, which occurs at a potential similar to that at which the oxidation of ascorbic acid and DOPAC occurs. The limit of detection was 0.4 μM for dopamine, and sensors were stable for at least one week. While the approach was novel, the LOD was not particularly low and, in general, direct detection of dopamine was relatively easier. In a similar approach, Tsai and Chiu deposited MWCNTs, Nafion and tyrosinase on a GCE.[81] Tyrosinase catalyzes the oxidation of dopamine to dopamine-o-quinone, the reduction of which can be measured amperometrically. The LOD was only 0.5 μM, and the sensor was more complex than are sensors used for direct detection because enzyme activity had to be maintained.

Doping of CNTs with boron can improve the electronic, mechanical, and conductive properties of CNTs.[91] Boron-doped carbon nanotubes (BCNTs) should be advantageous for the determination of dopamine because of extra edge plane sites on the surface and more functionalized groups at the defect sites of CNTs. Edge plane sites have better binding and faster electron transfer for neurotransmitters.[95] Indeed, at a GCE with adsorbed BCNTs, dopamine and ascorbic acid exhibited separate oxidation potentials, and a LOD of 1.4 nM was observed for dopamine.[92]

In most aspects, the techniques for modification of graphene materials resemble those for CNT functionalization, and the sensor fabrication processes are also similar. Some studies have compared the performance of CNT- and graphene- based sensors. For instance, Alwarappan et al.[96] demonstrated that the density of negative charge present on the graphene surface was greater than that found in SWCNTs. In addition, the possibility of employing graphene for the electrochemical detection of important neurotransmitters (e.g., dopamine and serotonin) was evaluated and compared with the potential for use of SWCNTs for this purpose. In all these experiments, graphene exhibited a better sensitivity, signal-to-noise ratio, and stability than did SWCNTs. In addition, the graphene electrodes exhibited superior biosensing performance than did the SWCNTs toward dopamine detection in the presence of common interfering agents (e.g., ascorbic acid and serotonin). Some recent examples of graphene modification strategies for improving the performance of electrochemical sensing include noncovalent attachment by pyrene derivatives,[97, 98] covalent bonding with dienophiles,[99, 100] oxygen plasma treatment,[101] doping with heteroatoms,[102-105] and creation of graphene-inorganic oxide hybrids.[106-108]

In recent work, Keeley et al.[101] described the heterogeneous electron transfer properties of high-quality multilayer graphene (MLG) films grown by CVD on nickel and transferred to insulating poly(ethylene terephthalate) sheets. An oxygen plasma treatment was used to enhance the ET properties of the films by generating oxygenated fimctionalities and edge-plane sites and defects. A series of biologically relevant molecules, including dopamine, NADH, ascorbic acid, and uric acid, were employed to show the improved sensing characteristics of the treated films. Control experiments involving commercially available edge-plane and basal-plane pyrolytic graphite (EPPG and BPPG) electrodes helped to elucidate the different responses observed for each probe, and it was shown that, in certain cases, treated MLG provided a viable alternative to EPPG, hitherto considered to be the "best-case scenario" in carbon electrochemistry. This is the first comprehensive study of the electroanalytical

properties of pristine and functionalized CVD-grown MLG, and it will serve as an important benchmark in the clarification of electron transfer behavior at graphene surfaces, with a view to the development of novel electrochemical sensors.

Zhang et al.[102] reported a novel strategy for the synthesis of nitrogen-doped activated graphene aerogel/gold nanoparticles (N-doped AGA/GNs). First, the mixture of graphite oxide, 2,4,6-trihydroxybenzaldehyde, urea and potassium hydroxide was dispersed in water and heated to form a graphene oxide hydrogel. Then, the hydrogel was freeze-dried and reduced by thermal annealing in an Ar/H_2 environment in sequence. Finally, GNs were adsorbed on the surface of the N-doped AGA. The resulting N-doped AGA/GNs exhibited excellent electronic conductivity (2.8×10^3 S/m), specific surface area (1258 m^2/g), well-defined 3D hierarchical porous structure and significantly higher heterogeneous electron transfer kinetics compared to other graphene aerogel materials. The N-doped AGA/GNs could serve as a new sensing material for the electrochemical detection of hydroquinone (HQ) and o-dihydroxybenzene (DHB). Owing to the greatly enhanced electron transfer and mass transport, the sensor displayed ultrasensitive electrochemical response to HQ and DHB. Its differential pulse voltammetric peak current increased linearly with an increase in HQ and DHB concentrations from 5.0×10^{-8} to 1.8×10^{-4} M for HQ and 1×10^{-8} to 2.0×10^{-4} M for DHB. The detection limit was 1.5×10^{-8} M for HQ and 3.3×10^{-9} M for DHB. The sensor was applied successfully to the detection of HQ and DHB in real water samples with the spiked recovery in the range of 96.8% - 103.2%. The study also provided a promising approach for the fabrication of graphene aerogel materials with improved electrochemical performance, for potential application in the development of biosensors, electrocatalysts, and energy storage devices.

Zeng et al.[106] proposed a novel imprinting route for the preparation of a composite of SiO_2-coated GO and molecularly imprinted polymers (GO/SiO_2-MIPs). In this route, SiO_2-coated GO sheets were synthesized in a water-alcohol mixture by the sol-gel technique. Prior to polymerization, the vinyl groups were introduced to the surface of GO/SiO_2 through chemical modification with gamma-methacryloxypropyl trimethoxysilane (gamma-MAPS), which directed the selective polymerization on the GO/SiO_2 surface. Then a novel composite of GO/SiO_2-MIPs was obtained successfully by copolymerization in the presence of the vinyl group-functionalized GO/SiO_2, dopamine, methacrylic acid and ethylene glycol dimethacrylate. The DPV current response of the GO/SiO_2-MIPs sensor was nearly 3.2 times that of the non-imprinted polymers (NIPs). In addition, the GO/SiO_2-MIPs sensor could distinguish DA from the relatively similar molecules of norepinephrine and epinephrine, while the sensors based on GO/SiO_2-NIPs and vinyl group-functionalized GO/SiO_2 did not exhibit such selectivity. The GO/SiO_2-MIPs sensor had a wide linear range over DA concentration from 5.0×10^{-8} to 1.6×10^{-4} M with a detection limit of 3.0×10^{-8} M. The sensor based on this novel imprinted composite was applied to the determination of DA in injections and human urine samples with satisfactory results.

It is important to emphasize that graphene is a biocompatible nanomaterial,[109] and, while serious toxicological effects were found with CNTs (mainly due to the presence of metallic impurities within them),[110] graphene is a non-toxic material. Another very important feature of graphene is the source materials. Graphene is fabricated mainly from graphite, which is inexpensive – the synthesis of CNTs, on the other hand, is expensive, as they are synthesized from carbon-containing gases with nanoparticles as templates. Furthermore, graphene provides more

uniform electroactive site distribution, greater densities, with over-potentials lower than those obtained with graphite, and larger surface areas (even larger than those of SWCNTs) for immobilization of biomolecules.

Electrocatalysis

Electrospun CNFs are promising support materials for catalytically active metal species for electrocatalysis applications. CNFs provide easier electron transfer along the continuous conductive fibers than do disconnected carbon systems (e.g., carbon particles) where the interfacial resistances between the individual carbon entities may be significant. However, electrospun CNFs can seldom be used as electrocatalysts on their own; one notable exception is nitrogen-doped CNFs. [111] Examples of utilizing carbon nanomaterials for the development of electrocatalysts are shown in **Figure 2**.

A series of studies by Li *et al.*[112-114] investigated Pt deposited through several methods on electrospun CNF mats for direct methanol fuel cell (DMFC) applications. The carbon nanofibers improved the catalytic peak current of methanol compared to that observed with commercial Pt/C, indicating that the 1D structure of the CNF mat is beneficial to the performance of the catalyst. In one of the Li reports,[113] the Pt clusters were electrodeposited on the CNF mats using multiple CV scans. Prior to Pt deposition, the as-synthesized CNFs exhibited a smooth surface and relatively uniform diameter ranging from 130 to 170 nm (**Figure 2a**). After CV electrodeposition, Pt clusters with irregular shapes and sizes from 50 to 200 nm were dispersed on the surfaces of the carbon fibers; the fibers in the inner layers of the mat were also coated with Pt clusters (**Figure 2b**). These Pt clusters were formed by small Pt nanoparticles (5 – 10 nm, **Figure 2c**, indicated by arrows) at the interface between the Pt and the carbon surfaces (**Figure 2c**). **Figure 2d** shows the CVs for methanol oxidation (1 M CH_3OH in 0.5 M H_2SO_4) using different catalyst systems. The unmodified CNF mat showed no significant redox activity. In the forward scan, Pt/CNF showed a much higher peak current density than did a commercial Pt/C electrode. This indicates that the Pt/CNF shows a significantly higher activity for methanol oxidation. In the reverse scan, both electrodes also showed anodic currents due to the removal of the incompletely oxidized carbonaceous species formed in the forward scan.

Another approach for Pt deposition reported by Lin *et al.*[115] involved the pre-functionalization of the CNFs with 1-aminopyrene in order to improve Pt attachment. After chemical reduction, they obtained Pt-Ru nanoparticles with small diameter (3.5 nm) and homogeneous distribution. The resultant Pt-Ru/CNFs had high electrochemical surface area and good activity toward methanol oxidation.

An alternative method for the fabrication of Pt/carbon and Pt–Pd/carbon composite nanofibres has been described by Lin *et al.*,[116, 117] where Pt and Pt-Pd nanoparticles were electrodeposited directly onto electrospun CNFs. In this method, the morphology and size of nanoparticles can be controlled *via* the deposition time. Huang *et al.*[118] have also used electrodeposition to prepare CNF-supported bimetallic Pt_xAu_{100-x} electrocatalysts, which showed good electrocatalytic performance for potential use in direct formic acid fuel cells.

Electrospun CNFs have also been used in alkaline fuel cells (AFCs). For instance, iron / cobalt / carbon electrospun nanofiber (FeCo/CNF) composite electrocatalysts demonstrated electrocatalytic activity and stability comparable to those of commercial carbon-supported platinum (Pt/C) for oxygen reduction reaction (ORR),

a direct 4-electron reduction pathway, and better ethanol tolerance than Pt/C in an alkaline electrolyte.[119] This approach opens up the possibility to prepare advanced cathode materials for AFCs without requiring noble metal catalysts.

In most cases, CNFs need to be functionalized with metal species in order to be used as electrocatalysts. However, heteroatom-doped CNFs have been found to exhibit catalytic activity to a certain degree. Thus, the preparation of low-cost metal-free catalytic systems based on CNFs may be possible. N-doped CNF electrodes, prepared by a floating catalyst CVD of ferrocene and either xylene or pyridine, exhibited electrocatalytic activities for ORR via a two-step two-electron pathway, and a greater than 100-fold increase in catalytic activity for H_2O_2 decomposition under both neutral and alkaline conditions, albeit with less activity than a Pt catalyst.[111] A strong correlation between the ORR peak potential and the nitrogen doping level was also observed; ORR peaks shifted about +30 mV per 1 atom% nitrogen incorporated.

CNTs can be used both as a catalyst support and as a metal-free catalyst. The high specific surface area, high mesoporosity, high electrical conductivity, high mechanical strength, and high corrosion resistance of CNTs make them very promising as a class of catalyst support materials for both DMFCs and proton exchange membrane fuel cells (PEMFCs).

For hydrogen PEMFCs, it has been shown that a CNT supported Pt catalyst with 12 wt% Pt loading could give a 10% higher fuel cell voltage and twice the power density compared to a carbon black-supported catalyst with 29% Pt loading.[120] MWCNT-supported Pt catalysts showed better performance in DMFCs compared to carbon black (XC-72) -supported catalysts both in half cell and full cell testing.[121] This report showed a mass activity of 14.7 mA/mg (Pt) for a Pt/MWCNT catalyst at 0.7 V vs. the dynamic hydrogen electrode (DHE), much higher than that of 2.2 mA/mg (Pt) for a Pt/XC-72 catalyst. SWCNT-supported Pt electrodes were also reported to exhibit higher catalytic activities for both methanol oxidation and ORR than unsupported Pt electrodes.[122] The onset potential of methanol oxidation on the nanotube electrode was 200 mV lower than that on the unsupported Pt electrode (400 mV vs. the standard calomel electrode, SCE). The higher catalytic activity was attributed to the larger surface area of the CNT architecture and the lower overpotential for methanol oxidation.

The high mechanical strength and superb corrosion resistance of CNTs provide excellent durability for the nanotube electrode. Compared to XC-72, MWCNTs were found to be electrochemically more stable, with less surface oxide formation and 20% lower corrosion current. Due to their high corrosion resistance, CNTs showed lower loss in Pt surface area and ORR activity. After 168 h oxidation treatment, the size distribution of Pt nanoparticles on XC-72 became broader and the average particle size became larger. In contrast, Pt particles on MWCNTs barely showed any increase in size. [122]

Compared to the randomly oriented CNTs, vertically aligned CNTs (VA-CNTs) with well-defined high surface area as well as good electrical and mechanical properties offer additional benefits as supporting electrodes in fuel cells. The improvement has been attributed to better Pt utilization and mass transport from the oriented CNT structures. Pt and Pt-alloy catalysts have been deposited on VA-CNTs for hydrogen PEMFC[123] and DMFC[124] applications.

In order to solve the CO poisoning problem for DMFCs, Ahn et al.[125] deposited a Pt-Ru binary catalyst with a Pt-random CNT catalyst on a 3D CNT array electrode prepared by an anodic aluminum oxide template. With the presence of Ru in the catalyst, the Pt-Ru/CNT electrode efficiently eliminated the CO poisoning.

The surface chemistry of support materials can also greatly affect the performance of the resultant catalysts. The interaction between the support and the catalyst can modify the electronic structure of catalyst metals, which in turn changes the catalytic activity[126] and durability of the catalysts.[127, 128]

Strongly coupled hybrid systems of inorganic nanoparicles and CNTs have also been shown to exhibit synergistic electrocatalytic activities.[129, 130] For instance, Liang et al.[130] synthesized CoO/N-doped CNT (NCNT) hybrids and demonstrated their ability to catalyze ORR. Scanning electron microscopy (SEM) images showed the formation of nanoparticles on CNTs with almost no nanoparticle detachment (**Figure 2e**). The lattice fringes of the nanoparticle from the high-resolution transmission electron microscopy (TEM) image (**Figure 2f**) are consistent with the CoO crystal structure. The high-resolution images also reveal that the graphitic carbon nanotube inner walls in the hybrid are undisrupted and continuous, suggesting that the inner walls of CNTs are not destroyed during the hybrid synthesis. The ORR activity of the CoO/NCNT hybrid was evaluated by CV. **Figure 2g** shows that the hybrid exhibits an ORR onset potential of 0.93 V and a peak potential of 0.86 V versus the reversible hydrogen electrode (RHE) in 1 M KOH, which are much more positive than those of the pure NCNT control. The higher catalytic activity in the hybrid can also be appreciated from the higher peak current density.

Another important research direction is the use of modified CNTs as metal-free catalysts in fuel cells. VA-CNTs formed by CVD of certain metal heterocyclic molecules, such as ferrocene/NH_3, exhibit ORR catalytic activity, which is attributed to the presence of FeN_2-C and/or FeN_4-C active sites in the nanotube structures.[131] Gong et al. showed that VA-NCNTs could act as highly effective metal-free ORR electrocatalysts even after complete removal of the residual Fe catalyst, demonstrating that the ORR activity of VA-NCNTs is solely due to the nitrogen doping.[132] Doping with other elements with electronegativity lower than that of carbon, such as boron, phosphorous, and sulfur, has also been demonstrated to give rise to a high ORR activity.[133, 134] Moreover, co-doping with more than one type of element has been found to bring about synergistic effects toward ORR.[135, 136] In addition, electron-accepting polyelectrolyte-modified CNTs have been demonstrated to be efficient metal-free electrocatalysts with strong ORR activities.[137]

In most cases, the strategies employed for CNT modifications can also be applied to graphene materials. N-doped graphene films produced by CVD in the presence of ammonia have been found to show an excellent ORR performance, comparable to that of VA-NCNTs with the same nitrogen content in alkaline medium.[138] A novel strategy to synthesize N, S-doped graphene was developed through one pot reduction of graphene oxide by microbial respiration of sulfate-reducing bacteria under mild conditions.[139] The N, S-doped graphene demonstrated significantly improved electrocatalytic properties and electrochemical sensing performances in comparison with single-doped graphene due to the synergistic effects of dual dopants on the properties of graphene. Strongly coupled graphene/inorganic nanoparticle hybrid systems have also been shown to exhibit electrocatalytic activities,[140] while polyelectrolyte-functionalized graphene has been used as a metal-free electrocatalysts for ORR.[141] In this latter study, poly(diallyldimethylammonium chloride) (PDDA) was used as an electron acceptor

for functionalizing graphene to impart electrocatalytic activity toward ORR. The adsorption of PDDA onto the surface of graphene occurred during the process of reducing graphene oxide (GO) to graphene by $NaBH_4$ in the presence of PDDA. Upon reduction, the color of the suspension changed from the yellow-brown of GO to black for graphene and PDDA-graphene (**Figure 2h**). Subsequent adsorption of PDDA made the surface of graphene positively charged, leading to a good dispersion *via* electrostatic repulsion among individual graphene sheets. In the absence of PDDA, the $NaBH_4$-reduced graphene precipitated and settled to the bottom of the vial (**Figure 2h**). The reduction of GO and concomitant functionalization of the resultant graphene with PDDA were further followed by FTIR spectroscopic measurements. As shown in **Figure 2h**, the FTIR spectrum of GO shows a strong peak at around 1630 cm^{-1} attributable to aromatic C=C, along with peaks characteristic of C=O stretching (1720 cm^{-1}), carboxyl (1415 cm^{-1}), and epoxy (1226 cm^{-1}). The reduction of GO to graphene is evidenced by the dramatic decrease in peak intensity at 1720, 1415, and 1226 cm^{-1}. Meanwhile, functionalization of graphene with PDDA is indicated by the appearance of new peaks at around 850 and 1505 cm^{-1}, attributable to the N–C bond in the adsorbed PDDA. **Figure 2i** shows the Raman spectra for graphene oxide, graphene, and PDDA–graphene. As expected, GO displays two prominent peaks at 1585 and 1351 cm^{-1} corresponding to the G and D bands, respectively. The D/G intensity ratio increased slightly from GO to graphene, suggesting a decrease of sp^2 domains induced by the $NaBH_4$ reduction. Upon PDDA adsorption, the G band of graphene up-shifted from 1585 to 1594 cm^{-1}, indicating the occurrence of electron transfer from graphene to the adsorbed PDDA. **Figure 2j** shows that the onset potential of ORR for the pure graphene electrode was at −0.25 V (versus SCE) with the cathodic reduction peak around −0.47 V (versus SCE). Upon functionalization of graphene with PDDA, both the onset potential and the ORR reduction peak potential shifted positively to around −0.15 and −0.35 V, respectively, accompanied by a concomitant increase in the peak current density. These results clearly demonstrated a significant enhancement in the ORR electrocatalytic activity for the PDDA–graphene with respect to the pure graphene electrode. The observed ORR electrocatalytic activity induced by the intermolecular charge transfer provides a general approach to various carbon-based metal-free ORR catalysts for oxygen reduction.

Supercapacitor Applications

Electrospun CNFs, which can be fabricated with varying fiber diameter, porosity and surface chemistry, enjoy several advantages for the improvement of capacitor performance.[142] Kim *et al.* first reported the application of electrospun carbon nanofibers to the development of supercapacitor devices.[143] Following this report, several other groups developed various modifications and new fabrication methods to improve the electrochemical properties of electrospun carbon nanofibers for supercapacitor applications.[118-126]

Improvements in the electrochemical capacitance of electrospun carbon nanofibers have been achieved through manipulation of fiber morphology and degree of graphitization by control of heat treatment conditions, [143] use of catalysts during carbonization and/or activation, [144, 145] and selection and combination of different polymer precursors such as PAN/CA,[146], PAN/PVP,[147] and PAN/pitch.[148]

Incorporation of redox-active species into electrospun carbon fibers can improve significantly their electrochemical capacitance due to the simultaneous use of two charge storage mechanisms: electrical double layer and

redox reactions. Ruthenium-embedded carbon nanofibers were prepared by the processes of stabilization, carbonization, and activation of fibers obtained by electrospinning a solution of ruthenium (III) acetylacetonate and PAN in dimethylformamide (DMF).[149] The specific capacitance was enhanced greatly after incorporation of Ru nanoparticles into the carbon fibers. The capacitance of carbon nanofibers without Ru was 140 F/g whereas the value for the electrode with 7.31 wt% Ru was 391 F/g. This increase was attributed to the synergistic effects of enhanced electric double-layer capacitance as a result of the expansion of the average pore diameter as well as the added pseudocapacitance made possible by the well-dispersed Ru nanoparticles. Moreover, coating of polypyrole (PPy) on the MWCNT-loaded fibers resulted in a further increase in capacitance due to the pseudocapacitive contribution from the electrochemically active polymer PPy.

Improvement of electrical conductivity by encapsulation of highly conductive components such as CNTs and metallic nanoparticles is another approach to enhancing the electrochemical performance of electrospun CNFs. **Figure 3** shows some uses of carbon nanomaterials for the development of supercapacitors. Electrospinning can produce CNT-embedded nanofibers in the form of a non-woven web.[150, 151] Guo et al.[151] prepared CNT-loaded carbonized electrospun nanofiber mats (CENMs) (**Figure 3a, 3b**). These authors found that the CNT-containing sample shows a much lower internal resistance (IR) drop than does the control sample without CNTs (**Figure 3c**). **Figure 3d** shows that the CNT-containing CNF mat exhibited significantly higher specific capacitance compared to that of the control sample at various current densities. This difference has been attributed to the improved conductivity and increased surface area due to incorporation of nanotubes. In addition, silver nanoparticle-containing carbon nanofibers were prepared through electrospinning of a mixture of silver powders and PAN in DMF, followed by stabilization in air at 250 °C for 2 h and carbonization in N_2 at 1000 °C for 2 h.[152] A ten-fold decrease in resistance was observed when 1 wt % silver nanoparticles were incorporated into the carbon fibers, compared to the case without silver loading. Only slight improvement in conductivity was found when the silver concentration was further increased to 5 wt%. For the 1 wt% silver concentration, the resistance was 4.5 $\times 10^{-2}$ Ω·cm, and for 3 wt% and 5 wt%, it was 4.0 $\times 10^{-2}$ and 3.5$\times 10^{-2}$ Ω·cm, respectively. However, when the silver content increased from 0 to 1 to 3 to 5 wt%, the specific capacitance of the carbon nanofiber webs was enhanced significantly from 190 to 224 to 234 to 248 F/g.

CNTs are attractive electrode materials for developing high-performance supercapacitor devices owing to their high electrical conductivity, high charge transport capability, and high electrolyte accessibility. Randomly entangled CNTs were the first type of CNT material explored for supercapacitor applications. Compared to high surface area activated carbon, CNTs have moderate specific surface areas. Nonetheless, capacitances that are higher than those of activated carbons have been reported (102 F/g for MWCNTs,[153] and 180 F/g for SWCNTs), in contrast to only tens of F/g for activated carbons. Based on the commonly realizable charge densities of 20 – 50 μF/cm^2 for electrical double-layer capacitors,[154] An et al.[155] estimated the theoretical capacitance for their CNTs (specific surface area: 357 m^2/g) to be around 71 – 178 F/g, in good agreement with the observed values (180 F/g) in the upper bound; this agreement indicates near perfect electrolyte accessibility for the CNTs. The mesoporosity induced by the tube entanglement is responsible for the high electrolyte accessibility. This

SWCNT-based supercapacitor showed a promising power density of 20 kW/kg with a maximum energy density of 10 Wh/kg (based on the mass of the active materials). A power density of 8 kW/kg with a maximum energy density of 1 Wh/kg has been realized for a packaged supercapacitor fabricated from MWCNT electrodes.[153] These power densities are higher than those obtained from activated carbon-based commercial devices,[156] but there is still room for improvement in energy density.

One way to improve the energy density of CNT-based supercapacitors is through incorporation of pseudocapacitive materials (e.g., redox polymers[17, 157, 158] and metal oxides[159-161] in most cases).[162] For example, Mao et al.[17] showed that a polyvinylferrocene (PVF)/CNT hybrid had a much higher specific capacitance and energy density than did each of the individual components alone. The PVF/CNT hybrid can be prepared by an efficient, low-cost, solution-based process, and the nanostructures and electrochemical performance of the hybrid can be easily varied by adjusting the composition of the precursor solution before deposition. Zhang et al.[159] grew manganese oxide (MO) "nanoflowers" on CNT arrays (CNTAs) (**Figure 3e, 3f**). The resulting composite exhibited capacitive CV behavior at different scan rates (**Figure 3g**). More importantly, the MO/CNTA displayed a much better rate performance when compared with other control samples, such as MO/activated carbon, CNTA, and MO/entangled CNT (ECNT), due to the vertical alignment of CNTs in the MO/CNTA system that allows for fast electrolyte transport.

Due to its large surface area, high carrier transport mobility and excellent thermal/mechanical stability, graphene has recently been studied as the basis for an alternative carbon-based electrode in supercapacitors.[163] Theoretically, the double-layer capacitance value for a graphene electrode can reach up to 550 F/g, the highest value of intrinsic capacitance among all carbon-based electrodes.[164] Using chemically modified graphene oxide electrodes, Stoller et al. obtained specific capacitances of 135 and 99 F/g in aqueous and organic electrolytes, respectively.[165] Zhu et al.[5] synthesized activated, microwaved, exfoliated GO (a-MEGO) (**Figure 3i, 3j**) with a BET surface area of 3100 m^2/g. The high-resolution image (**Figure 3k**) shows that the a-MEGO piece contains a dense network of nanometer-scale pores surrounded by highly curved, predominantly single-layer graphene. **Figure 3l** shows that the a-MEGO based supercapacitor exhibits nearly rectangular CV profiles from 0 to 3.5 V over a wide range of scan rates. Additionally, by using simple microwave heating and propylene carbonation solution methods for exfoliation and reduction of graphene oxide, the same group also obtained capacitance values of 191 and 120 F/g, respectively.[166, 167] Recent work has focused on combining graphene with pseudocapacitive materials for enhanced energy densities and rate capabilities.[162, 168, 169]

Heteroatom doping is another promising approach to enhancing the electrocapacitive performance of CNTs and graphene materials. Lee et al.[170] showed that N-doping improved the specific capacitance of macroporous graphene films, by enhancing the electrical conductivity and wettability. Redox-active pyridinic or pyrolytic N can also give rise to pseudocapacitance.[171-174] Doping with other heteroatoms to improve supercapacitor performance is relatively less explored. Recently, Han et al.[175] reported the energy storage properties of B-doped graphene. Synergistic effects from co-doping with B and N to improve electrocapacitive performance have also been reported.[172, 176]

Lithium Ion Battery Applications

Carbon nanomaterials have been used in the development of LIBs; some examples are given in **Figures 4**. Carbonaceous materials exhibit Li^+ storage capabilities; thus various carbon forms, including carbon particles, CNFs, CNTs and graphene, have been investigated for LIB applications. Compared to natural graphite, which has a relatively low theoretical Li^+ storage capacity of 372 mAh/g, PAN-derived electrospun CNFs thermally treated at 1000 °C have been found to exhibit a slightly higher, reversible, discharge capacity of 450 mAh/g.[177] However, higher temperature treatment (2800 °C) led to a remarkable decrease in the LIB reversible capacity. To improve LIB performance, it is often necessary to incorporate into the carbon matrix another component that has a high Li^+ storage capacity, such as silicon (Si) or tin (Sn).

Si has been considered an excellent candidate for next-generation LIB anode materials since it has the highest known theoretical capacity of 4200 mAh/g, significantly greater than the values for graphite and metal oxides.[178, 179] However, Si can experience large volume changes, leading to severe pulverization upon lithium insertion and extraction, which results in reduced capacity and cycling stability.[180] Dispersion of Si nanoparticles in a carbon matrix, which acts as both a structural buffer and an electroactive material, proves to be an effective strategy to improve the LIB performance of Si. The electrospinning of PAN and Si in DMF, followed by thermal treatment, resulted in carbon nanofibers with Si nanoparticles distributed both inside and on the surfaces of the fibers. These Si/C fibers were found to have good capacitive retention when tested as LIB anode materials.[181, 182] Porous carbon nanofibers containing Si nanoparticles that were prepared through carbonization of composite nanofibers of PAN, polylactic acid (PLLA) and Si exhibited large reversible capacity and relatively good cycling performance with a high current density of 200 mAh/g.[183]

Metallic tin (Sn) has also attracted tremendous interest as an anode material for LIBs due to its relatively high theoretical capacity of about 990 mAh/g. Practical applications of Sn to LIBs are hampered by poor cycling stability due to the substantial volume changes that occur during charging and discharging. Electrospun carbon fibers with dispersed tin nanoparticles have been shown to improve the cycling stability of tin anodes considerably. "Sn@C" nanoparticles (comprising a Sn core wrapped by a thin, 10nm carbon layer) encapsulated in bamboo-like hollow carbon nanofibers (**Figure 4a-4d**) were synthesized by carbonization of coaxially electrospun nanofibers.[184] Specifically, the Sn@C composite fibers were prepared by the electrospinning of PAN nanofibers containing tributyltin (TBT) dissolved into a mineral oil, followed by extraction of the mineral oil, most of which was located in the cores of the fibers, by *n*-octane, and finally by heating the fibers at 1000 °C in an Ar/H_2 atmosphere to carbonize the outer PAN shell and to decompose the TBT core to metallic Sn. The Sn/C composite electrode was compared to a commercial Sn nanopowder electrode in terms of cycling performance (**Figure 4e**). The Sn/C composite electrode exhibited improved cycling performance and a high reversible specific capacity of over 800 mAh/g for the first 10 cycles, while maintaining a reversible capacity of about 737 mAh/g after 200 cycles. In contrast, the Sn nanopowder electrode had a discharge capacity that dropped rapidly after the first 40 cycles.

Another type of Sn/C composite electrode, porous multichannel carbon microtubes (SPMCTs) with Sn nanoparticles encapsulated, was prepared via the single-nozzle electrospinning of poly(methyl methacrylate) (PMMA)/PAN/tin octoate precursor solution and subsequent carbonization to remove PMMA and reduce tin ox-

ide to tin nanoparticles.[185] The SPMCT electrode also showed significantly improved cycling performance compared to the electrode made of Sn nanopowder alone. To improve LIB performance, other electrochemically active metallic particles such as Co,[186] Fe,[187], Mn,[181, 188] Ni[189], and Cu[190] have also been incorporated into electrospun CNFs.

CNTs are also attractive host anode materials for Li ion intercalation[191, 192]. Lithium incorporation into CNT lattices has been the subject of a number of theoretical studies, as discussed later in the section entitled [193].

It has been assumed that a large amount of Li^+ can be stored in the central core, the interlayer space (for MWCNTs), or the empty space between the nanotubes when they are assembled in bundles. A reversible Li^+ intercalation capacity of as high as 400 mAh/g for MWCNTs has been reported.[194] The higher capacity of CNTs than that of graphite (372 mAh/g) is believed to be due to the higher specific surface area of CNTs. The capacity of CNTs can be further increased by opening or cutting the CNTs. Shimoda et al.[195] reported a reversible capacity of 700 mAh/g for SWCNTs that were etched by strong acids to open the tubes and reduce their length. There is a clear morphological difference between the SWCNTs before (**Figure 4f**) and after (**Figure 4g**) the acid treatment. **Figure 4h** demonstrates that the lithium storage capacity per carbon atom increased with a decrease in nanotube length; the saturation ratio increased from Li/C = 1/6 to Li/C = 1/3. In another report, Gao et al. [195] achieved a reversible capacity of 1000 mAh/g for their SWCNTs by ball milling. Heteroatom doping is expected to improve the charge transfer and lithium diffusion in CNTs. For example, Shin et al.[196] reported an extremely high capacity of 3500 mAh/g with N-doped CNTs. N-doped sites on the carbon nanotubes provide extrinsic defects for enhanced lithium diffusion into the inter-wall space, favorable binding sites for the lithium ion, and addition functional sites for further capacity boost.

Although CNTs and other negative electrode nanomaterials have been shown to exhibit similar or better capacities compared to graphite in commercial Li ion batteries, they do not improve on graphite's rate capability.[197] Several studies suggest that alignment of CNTs allows for better contact with the current collector and facilitates ion diffusion to improve bulk electron transport properties, thereby leading to improved rate capabilities.[198-200] CNTs have also been explored as conductive additives for various cathode material systems, such as $LiCoO_2$,[201] $LiFePO_4$,[202] and V_2O_5.[203]

Graphene has also been investigated as a promising electrode material for Li-ion batteries due to its high electrical conductivity, large surface area and good electrochemical stability. However, the specific capacity of graphene is relatively low because every six carbon atoms can hold only one Li ion.[204] Common methods to overcome this major drawback include creation of hybrids with metal oxides,[205-210] incorporation of chemical dopants,[211-213] and control of layer structures.[214, 215]

The main purpose of developing hybrids with graphene and metal oxides for anode materials is to utilize advantages of both these components. Metal oxide anodes have a main drawback, which is the large volume change during the charge/discharge process, leading to cracking of electrodes and poor reversibility; however, metal oxides possess larger Li ion storage capacities than do carbon materials. In composites, graphene acts as a mechanical support to relieve the cracking, and also as a conductive layer to promote electron transport. Wang et al.[207]

developed a solution-based process to synthesize hybrids consisting of Mn_3O_4 nanoparticles and reduced graphene oxide (rGO) (**Figure 4i**) for LIB applications. XRD profiles (**Figure 4j**) confirm the presence of Mn_3O_4 in the hybrid. The peak widths indicate that the size of the nanoparticles was around 10 – 20 nm. The hybrid system showed a high specific capacity up to ~900 mAh/g, close to the theoretical capacity, with good rate capability and cycling stability (**Figure 4k**), owing to the strong interactions between the graphene substrate and the Mn_3O_4 nanoparticles grown atop. Alternatively, heteroatom doping of graphene has also been shown to improve its LIB performance. For instance, Wu et al.[212] reported the use of N- and B-doped graphene for anode materials. Their devices displayed a high capacity of 1043 mAh/g for N-doped graphene and 1549 mAh/g for B-doped graphene, with significantly improved Coulombic efficiency, power density and cycling performance. Additionally, Wang et al.[216] have shown that N-doped graphene nanosheets exhibit excellent rate performance for LIB applications. Another recent work reported synergistic effects for lithium storage from co-doping of N and S.[217]

How Electronic Properties of Carbon Materials Affect Their Electrochemical Activities

A crucial and intrinsic factor governing the performance of electrode materials is their electronic structure. The DOS varies greatly for different forms of carbon. The high conductivity of metals originates from the combination of a large number of atomic orbitals to form bands with a high DOS. Electrons move freely with changing energy, and metallic conduction obeys Ohm's law. Conservation of energy dictates that the electron transfer process between an electrode and a redox system is fastest when the energy of the electrons is equal in the electrode phase and in the thermally activated redox species. A high DOS in the electrode material increases the likelihood that an electron of the correct energy is available for electron transfer to a redox system; therefore, the hetereogeneous electron transfer rate is dependent on the DOS of the electrode material.[218] Semiconductor electrodes represent the opposite of a metallic DOS: there are no electronic states in the gap region, and the electron transfer process does not generally happen between a semiconductor electrode and redox systems with E^0 values in the gap region. Metallic electrodes generally have a high DOS. For instance, gold enjoys a high DOS of 0.28 states $atom^{-1}$ eV^{-1}, and this value remains almost invariant with energy.[219] In contrast, the DOS for highly oriented pyrolytic graphite (HOPG) at the potential of zero charge (PZC) is 0.0022 states $atom^{-1}$ eV^{-1}.[220]

In contrast to the high DOS with only weak energy dependence, observed for metals, both the shape and magnitude of the DOS distribution for carbon materials vary remarkably with carbon structure. Such a phenomenon allows for adjustment of electronic structures of carbon through manipulation of the atomic bonding structure. The DOS distribution for HOPG is shown in **Figure 5a**, and an expansion of the region near the Fermi level is shown in **Figure 5b**.[221] The σ and π orbitals of the graphitic carbons combine to form the filled valence bands, which are shaded in **Figure 5a**, while antibonding orbitals comprise the conduction band. For an infinite graphene sheet or ideal graphite crystal, there is a small overlap of the valence and conduction bands, leading to a low DOS at the Fermi level. HOPG is considered a semi-metal, while disordered graphite behaves electronically like a metal with a low DOS. Even with some disorder to increase the DOS near the Fermi level, the lower conductivity of graphite materials compared with metals is at least partially a consequence of the low DOS.

CNTs have a variety of DOS distributions, which depend on tube diameter. **Figure 5c** shows an example,[222] plotted in the format developed by Gerischer for semiconductor electrochemistry.[223] The DOS of a semiconducting nanotube is shown in the left portion of **Figure 5c**. It exhibits much more structure than does graphite.[222] Semiconducting CNTs have no electronic states in the gap region, while metallic CNTs have a nonzero DOS both above and below the Fermi level. In the case shown in Figure 5c, oxidation occurs when the distribution of electron energies in the reduced material, W_{red}, overlaps with an unfilled level in the CNT, as shown by the red arrow. As with semiconducting electrode materials, electron transfer does not occur for the molecule whose electron energy levels are within the gap region.

Graphene is intrinsically a semi-metal or zero-gap semiconductor. The valence band structure of graphene combines semiconducting and metallic characteristics, and can be conceived either as a metal with a vanishing Fermi surface or as a semiconductor with a vanishing band gap.[75] This peculiar feature stems from the honeycomb lattice of graphene, comprised of two equivalent carbon sublattices A and B, and cosine-like energy bands associated with the sub-lattices. In this honeycomb lattice, the *s*, p_X and p_Y orbitals of carbon atoms form σ bonds with the neighboring carbon atoms, while the π electrons in the p_Z orbital, one from each carbon, form the bonding π and antibonding π^* bands of graphene. These π and π^* bands touch each other at the *K*-point in the Brillouin zone, which results in two conical points, *K* and *K*', per Brillouin zone where band crossing occurs (**Figure 5d**).[224] Near the *K* points, the bands have a linear dispersion relation, $E = hv_F|k|$, where *E* is energy, *k* is the wave vector, *h* is Planck's constant divided by 2π, and v_F is the Fermi velocity in graphene ($\sim 10^6$ m/s). This linear dispersion relation has similarities with that for massless photons, in contrast to the parabolic dispersion relation of electrons in conventional semiconductors. Additionally, at low energies near the K points, the electronic states have contributions from two sub-lattices that can be represented by spinors, resulting in a Hamiltonian that is reminiscent of the Dirac Hamiltonian in quantum electrodynamics (QED). The electron spin in the Dirac-like equation is represented by a new quantum number that is often called a "pseudo-spin" (in addition to the real spin of the electrons). The QED-like spectrum in graphene allows the observation of novel phenomena such as Klein tunneling[225] and anomalous quantum Hall effects.[226, 227] The linear dispersion and pseudo-spin are two central features of graphene that have led to the term "massless Dirac fermions" as a descriptor for carriers in graphene.[228]

The electronic properties of CNFs, CNTs and graphene govern their electrochemical activities for a variety of applications. For example, for the development of electrochemical sensors, the DOS of the electrode material determines the electron transfer efficiencies with the target molecules, and thus is important for improving sensitivity. An increase in the DOS can be achieved, for instance, by increasing nanographite concentrations in turbostratic CNFs[3] and controlled exfoliation of metallic carbon nanotubes.[229] For electrocatalysis applications, the doping of CNTs and graphene with heteroatoms to modulate their electronic structures and charge distributions proved to be the key to improved catalytic activities.[132] For supercapacitor applications, band structure engineering is an effective strategy to improve the charge-storage capabilities of CNTs and graphene materials.[230] For LIB applications, the geometrical features and electronic structures of CNTs significantly affect lithium adsorp-

tion and diffusion.[231, 232] Therefore, in the following section we discuss several cases in detail, to elucidate how the electronic properties of carbon nanomaterials affect their electrochemical activities. It should be pointed out that, although several other factors such as surface areas, surface chemistries, and pore structures may affect the electrochemical activities of the carbon electrodes, in the subsequent examples the electronic properties of carbon are the key determinant in the improved electrochemical performance.

Mao et al.[3] presented a simple and effective strategy to adjust the electrochemical activities of electrospun CNF webs via controlling their DOS by processing conditions. The DOS of electrospun CNFs was controlled by selecting an appropriate polymer precursor (PAN) to generate nanosized graphite domains upon carbonization, and then varying the thermal treatment conditions to adjust the concentration of these graphite domains. The CNF webs synthesized at carbonization temperatures of 1000, 1100, and 1200 °C are denoted as CNF1000, CNF1100, and CNF1200, respectively. When compared to large graphite domains, nanosized graphite domains with many edge-plane sites provide a significantly higher DOS near the Fermi level due to the overlap between the valence and conduction bands.[233] The concentration of nanometric graphite clusters in the CNF webs have a significant impact on their DOS. XPS results (**Figure 6a**) clearly show that from CNF1000 to CNF1100 to CNF1200 the maximum of the spectrum is shifted to lower binding energies. This shift indicates that graphite concentration increases with carbonization temperature since the sp^2 bond has a lower binding energy than the sp^3 bond, Electron energy loss spectra (EELS) of the CNF webs (**Figure 6b**) were used to estimate the ratios of π orbitals to σ orbitals. The peak from 280 to 288 eV and the band from 288 to 311 eV are due to excitation of electrons to the π* and σ* states, respectively. The ratio of the integrated areas under these two energy windows approximates the π/σ ratio, which is 1/3 and 0/4 for purely sp^2 and sp^3 bonded carbon, respectively. A higher π/σ ratio implies a higher graphite concentration. The π/σ ratios increase from 0.1097 to 0.1153 to 0.1383 for CNF1000, CNF1100 and CNF1200, respectively, indicating that the number of sp^2 bonds increases with carbonization temperature. Kinetic studies on both outer-sphere and inner-sphere systems show that the CNF webs exhibit controlled electrochemical activity for all species despite their differing kinetic sensitivities (**Figure 6c, 6d**). The CNF webs also showed different DET efficiencies with cytochrome c and horse radish peroxidase.[3]

To form devices, CNFs with a high DOS were deposited directly onto a conductive substrate (**Figure 7a**); such a fiber/substrate construct has been shown to be useful for the development of electrochemical sensors with ultrawide dynamic ranges.[67] **Figure 7b** shows the electroactive surface areas (ESAs) of the ECNF sensors with different electrospinning deposition times. The ECNF device with a deposition time of 12 h exhibits an ESA of 3.7 cm^2, a value that is significantly higher than that reported for electrochemical biosensors based on CNT assemblies (generally ~10^{-2} cm^2).[234] Additionally, there exists a linear correlation between the ESA values and the deposition time, which indicates that the ESA can be varied systematically using this fabrication process. As proof of principle, DA was used as a model analyte to evaluate the sensor performance. **Figure 7c** shows the nonlinear calibration curve obtained using a sensor with 12 h deposition time. Advanced carbon electrodes,[1] especially those based on CNTs[80, 82-84, 89, 235-241] and graphene,[229, 242-247] have been researched extensively for electrochemical DA detection, and the detection ranges of these DA sensors have been well-documented. The ECNF

sensors developed here demonstrate remarkably wider sensing ranges than reported previously for carbon-based sensors while exhibiting comparable detection limits.

Controlled oxidation of MWCNTs can modulate their electronic structure, thereby leading to improved sensing performance. Sun et al.[229] reported microwave-assisted synthesis of a core-shell MWCNT/graphene oxide nanoribbon (GONRs) heterostructure (**Figure 8a, 8c-8e**). CV measurements (**Figure 8b**) show that GONR/GC exhibits a much higher current density than does GC, MWCNT/GC, or graphene/GC. To explain the enhanced sensitivity, the authors employed X-ray absorption near-edge structure spectroscopy (XANES) to elucidate the electronic structure of GONR. XANES is a technique that interrogates photoexcitation for electrons from a core level (absorption edge) of an atom to levels within an energy range of ~50 eV above the absorption edge. It is characterized by intense resonance owing to excitations of core-level electrons to unoccupied orbitals and multiple scattering of the emitted photoelectrons by the geometrical arrangement of neighboring atoms.[248] XANES is sensitive to the local chemistry of the atom being detected; thus this technique is useful for investigating the chemical bonding, electronic structure, and interactions of the materials. **Figure 8f** shows the C K-edge XANES of GONRs and MWCNTs. From this figure, the authors claim that the GONR hybrid structure exhibits a higher concentration of edge defects and a higher unoccupied DOS than do MWCNTs. The difference in the electronic structure between GONR and MWCNTs is claimed to be responsible for the sensing performance disparity.

The doping of CNTs with heteroatoms has also been found to perturb their electronic properties, thus giving rise to high electrocatalytic activities towards ORR. Gong et al.[132] found that VA-NCNTs (**Figure 9a**) act as highly effective metal-free ORR electrocatalysts. Quantum mechanics calculations indicate that carbon atoms adjacent to nitrogen dopants of the VA-NCNTs possess a high positive charge density to counter-balance the strong electron affinity of the nitrogen atom (**Figure 9b**). The nitrogen-induced charge delocalization could change the electrochemical potential for ORR and the chemisorption mode of O_2 from the usual end-on adsorption (Pauling model) at the conventional CNT surface to a side-on adsorption (Yeager model) at the NCNT surface (**Figure 9c**).[132, 249] The parallel diatomic adsorption could effectively weaken the O-O bonding to facilitate ORR at the NCNT electrode. As such, doping CNT with nitrogen heteroatoms can efficiently create the metal-free active sites for electrochemical reduction of O_2. In alkaline electrolyte, the metal-free VA-NCNTs are able to catalyze a four-electron ORR process with a much higher catalytic activity, lower over-potential, and smaller crossover effects compared to commercially available Pt/carbon black catalysts (**Figure 9d**). Moreover, being nonmetallic, the VA-NCNTs are insensitive to CO poisoning. N-doped graphene (N-graphene) films produced by CVD in the presence of ammonia have been demonstrated to show a superb ORR performance similar to that of VA-NCNTs with the same nitrogen content in alkaline medium.[138] In addition to the intramolecular charge-transfer that impart ORR electrocatalytic activities to NCNTs and N-graphene discussed above, Wang et al.[137, 141] have shown that certain polyelectrolyte (e.g., PDDA) functionalized nitrogen-free CNTs and graphene could also act as metal-free electrocatalysts for ORR through the intermolecular charge-transfer from the all-carbon materials to the adsorbed PDDA (**Figure 10**).

Strong chemical coupling between inorganic nanoparticles and nanocarbons has been found to change significantly the electronic structure of each individual component; such changes have been shown to impart syner-

gistic electrocatalytic activities to the resulting hybrid systems.[108, 109, 114] The carbon K-edge, nitrogen K-edge, and metal L-edge XANES spectra can be used to elucidate the states of the carbon, nitrogen, metal atoms in these strongly coupled hybrids, respectively.

Liang et al.[140] synthesized a hybrid material system consisting of Co_3O_4 nanocrystals and reduced, mildly oxidized graphene oxide (rmGO) or nitrogen-doped rmGO (N-rmGO). **Figure 11a** shows a representative TEM image of the Co_3O_4/N-rmGO hybrid. The authors found that the Co_3O_4/graphene hybrids exhibit much higher ORR activities than do the two individual components alone (**Figure 11b**). Free Co_3O_4 nanocrystals, rmGO and N-rmGO alone show very poor ORR activities; in contrast, the Co_3O_4/rmGO and Co_3O_4/N-rmGO show much more positive ORR onset potentials and higher cathodic currents. The authors claim that the strong chemical coupling between Co_3O_4 and graphene leads to significant changes in the electronic structure of C, O and Co atoms. Therefore, the resulting hybrids exhibit much higher electrocatalytic activities towards ORR. **Figure 11c** shows that compared to N-rmGO, the Co_3O_4/N-rmGO hybrid exhibits a clear increase of C K-edge peak intensity at ~288 eV, corresponding to carbon atoms in graphene attached to oxygen or other species. This suggested the possible formation of the interfacial Co-O-C and Co-N-C bonds in the hybrid. In the O K-edge XANES (**Figure 11c inset),** an obvious decrease in unoccupied O 2p-Co 3d hybridized state (~532 eV) was observed, accompanied by an increase in the Co L-edge XANES peak (mapping of the unoccupied Co 3d projected state, see **Figure 11d**) in the hybrid compared to pure Co_3O_4 nanocrystal. This suggests a higher electron density at the O site and a lower electron density at the Co site, and consequently a higher ionic Co-O bonding in the hybrid. The $MnCo_2O_4$/N-rmGO[129] and CoO/N-CNT[130] hybrids show similar changes in the C K-edge spectra compared to their pure nanocarbon samples (**Figure 12**). These observations suggest that such electronic structure modulation is general in the inorganic nanoparticle/nanocarbon hybrids.

The electronic properties of carbon materials also have a remarkable impact on their LIB anode performance. As mentioned earlier, the electronic properties of semiconducting and metallic CNTs differ dramatically. Hence, it is expected that the electrochemical properties may differ, including the Li storage properties. In LIB devices, the electronic conductivity of the anode material plays a crucial role especially in granular media in order to bring the electronic carrier as rapidly as possible from the current collector to the electrolyte.[250] Kawasaki et al.[251] reported that the Li ion storage capacity of metallic SWCNTs is about five times higher than that of semiconducting tubes. Udomvech et al.[252] suggested that the nanotube chirality plays a key role in the Li-CNT interaction.

The lithium insertion level in CNTs is not limited to LiC_6 (as in the case for graphite). This is due to the vastly different morphologies. Shimoda et al.[195] estimated that a density up to about LiC_3 is possible; however, Chen *et al*. reported that the MWCNTs synthesized by them exhibit capacities lower than LiC_6.[253] The large variation in reported capacities is related to the different structures and morphologies of CNTs investigated. Particularly important to the capacity is the presence of defects. Nishidate et al.[254] have examined the effects of defects on lithium insertion in CNTs. **Figure 13a** shows that as carbon atoms are removed, a hole occurs in the wall of the carbon nanotube as each of the carbon atoms attempts to remain bonded with its neighbors. Note that n = 7, 8, 9 means 7, 8, 9 carbon ring defects, respectively. **Figure 13b** shows that while lithium rarely diffuses into defect-

free, n = 7, or n = 8 defected CNTs, lithium diffuses readily into n = 9 defected CNTs. Once inside, the lithium is able to move through the interior of the CNT and can be absorbed successfully, indicating that lithium ions can be accumulated in the interior of CNTs in addition to the exterior. Garau et al.[255, 256] performed *ab initio* calculations of the molecular interaction potential with polarization (MIPp) of CNTs of various chiralities interacting with lithium cations. Their studies show that topological defects that are 10-membered rings pose no barrier to lithium diffusion inside the CNT, and that 9-membered ring defects have a substantial diffusion barrier of 9.69 kcal/mol. These results appear to be consistent with the conclusion of Nishidate et al. that lithium easily diffuses into CNTs with n > 9 defects. While Nishidate et al. focused on defects on the sidewall of the CNT, it should be noted that lithium can also enter CNTs through the ends of CNTs,if they are open-ended rather than terminated by buckyball-like caps.[257]

The CNT diameter is another important factor that affects the lithium adsorption and diffusion, both inside and outside the CNTs.[231, 232] Intercalated lithium ions can interact with CNTs, and the charge transfer between lithium ions and CNTs can further enhance these interactions. The interaction is related to the curvature of the tubes, and results in different capacities for CNTs of different sizes. Liu et al.[231] conducted a first-principles study of lithium absorption in CNTs. Their Li-absorbed cluster models are shown in **Figure 14a**, with limited numbers of lithium atoms absorbed on both the inside and the outside of the nanotubes. The Li absorption energy and binding energy of CNTs are dependent on the CNT diameters. The first principles total energy calculations of Li absorption into CNTs with various diameters show that with an increase in tube diameter, the external Li absorption energy decreases while the internal Li absorption energy increases. In addition, when the tube diameter is small, the Li absorption energy for external absorption is larger than that of internal absorption. As for the binding energy, the values for both the pure and Li-absorbed nanotubes increase with the diameter. Zhao et al.[232] showed a clear relationship between the Li/C ratio and the tube diameter. With an increase in the tube diameter, the intercalated lithium atoms tended to form a multi-shell structure (**Figure 14b**) at the equilibrium state, composed of coaxial tubes with a linear chain in the axis, which improves the CNT capacity for lithium.

Similar to the cases involving CNTs, the electronic structure of graphene materials also have significant impacts on their lithium storage properties. Although pristine graphene can be used as the anode material in LIBs,[258, 259] modified graphenes with perturbed electronic structure show enhanced LIB performance.[167, 211-213] To tune the electronic properties of graphene, it is common to use chemical dopants. Both theoretical prediction and experimental results have indicated that chemical dopants such as nitrogen and/or boron in graphene materials exert a substantial influence on the specific capacity for lithium storage relative to pristine graphenes.[211, 212, 216, 260] In a typical example, nitrogen-doped graphene was grown directly on Cu foil by chemical vapor deposition using acetonitrile as the liquid precursor.[211] The study on the reversible lithium ion intercalation properties of NG suggested that its reversible discharge capacity is almost double that of pristine graphene, attributed to the presence of a large number of surface defects induced by nitrogen-doping. These results agree with previous theoretical predictions of the improved Li ion intercalation for pyridinic nitrogen-doped carbon nanotubes.[261] In another case, NG and boron-doped graphene (BG) were prepared by heat treatment of pristine CVD graphene in a gas mixture of NH_3/Ar (600 °C) and BCl_3/Ar (800 °C), respectively.[212] XPS shows that the doping content is

3.06% in NG and 0.88% in BG. Due to the relatively low thermal treatment temperature, nitrogen atoms in NG consisted mainly of pyridinic N and pyrrolic N. Interestingly, outstanding capacities of 1043 mAh/g and 1549 mAh/g were obtained for NG and BG, respectively, at a low charge/discharge rate of 50 mA/g. More importantly, even at an ultrafast charge/discharge rate of 25 A/g, the doped graphene retained a capacity of 199 mAh/g for NG and 235 mAh/g for BG.

Another approach to improve LIB performance is to combine different nanocarbons with different electronic properties. Yoo et al.[214] prepared graphene nanosheets (GNSs) by reducing GO with hydrazine hydrate. Since the accommodation of lithium in the layered electrode materials can be influenced by the layer spacing between the nanosheets, they further fabricated mixtures of GNS with CNT or C_{60} to tune the interlayer spacing of GNS. As a result, the d-spacings for GNS, GNS+CNT, GNS+C_{60}, were found to be 0.365, 0.40, and 0.42 nm, respectively. The increase in the d-spacing is attributed to the intercalation of other nanocarbons in GNS. Thus, reversible capacities of 540, 730, and 784 mAh/g were achieved for GNS, GNS+CNT, and GNS+C_{60}, respectively. These values are significantly higher than the capacity of graphite. This pronounced improvement is due to the different electronic structures of the nanocarbon hybrids from that of graphite, and to the additional sites for the accommodation of lithium ions induced by the expansion in the *d*-spacing of the graphene layers.

Summary and Outlook

Carbon-based sensors, electrocatalyts, supercapacitors and LIBs share electrochemical similarities to a certain degree; some carbon structural manipulation methods apply generally to each application area. For instance, modulation of electrochemical activities can be achieved by perturbation of electronic structure, by either covalent (e.g., controlled oxidation, doping with heteroatoms, manipulation of synthesis conditions) or noncolvent methods (adsorption of surfactants or polyelectrolytes). Additionally, architectural design plays a significant role in the overall electrochemical performance. For example, substrate supported continuous CNFs with good mesh integrity exhibit wide-range sensing capabilities, and vertically aligned CNTs and graphene sheets show good rate performance and high sensitivities. In short, the general principles for improving the performance of these carbon-based electrochemical devices include: (1) incorporation of additional non-carbon components that exhibit electrochemical activities towards a specific application; (2) manipulation of the intrinsic electronic properties of carbon such as DOS and band structure; and (3) design of complex multilevel structures to facilitate electron transport and ion diffusion simultaneously. However, there is still considerable scope for more research into the fundamentals of carbon electrochemistry. For instance, special attention should be devoted to the estimation of electron transfer kinetics on heterogeneous carbon surfaces (i.e., surfaces composed of areas with different electronic properties), the interpretation of the electron transport properties at the graphene/substrate and graphene/solution interfaces, the determination of the charged impurities in carbon electrodes, and the understanding of the exact doping configuration that contributes to the high electrocatalytic activities of doped nanocarbons. Furthermore, these research directions would benefit from the development of new characterization techniques such as in situ electrochemical microscopy and spectroscopy, and from advances in theoretical studies on electronic properties of modified carbon structures.

Although each class of carbon nanomaterials may ultimately impact each of these applications areas, the unique characteristics of electrospun CNFs, CNTs, and graphene suggest that they will have disproportionate representation in electrochemical devices that play to their individual advantages. For instance, electrospun CNFs are often used as conductive supports for Pt and Sn/Si in electrocatalysis and LIB applications, respectively, mainly because of the ease of incorporating precursor species in the electrospinning solutions. Well-established relations between the electronic structures of CNTs and graphene and their electrochemical activities allow these materials to be used extensively as metal-free catalysts and sensing materials.

While significant progress has been achieved, additional challenges must be addressed before the full commercial potential of carbon nanomaterials is realized. Device-to-device variability remains an issue for almost all types of electrochemical devices. Many variables need to be tested and then optimized to create a commercial device. Electrochemical performance can depend on the method of electrode attachment, and the eventual architecture of the device. Detailed description of the device fabrication procedure is necessary if results are to have any meaning.

In addition, the ability to scale-up manufacturing processes for the electrochemical devices needs to be taken into consideration. The state-of-the-art electrospinning techniques (e.g., multiple-nozzle and free surface, or needleless, electrospinning[262]) can produce ultrafine fiber mats with high productivity and reproducibility. However, for creating multilevel structures (e.g., core-shell structure and nanoparticle-decorated fibers), specially designed multi-fluidic nozzles or multi-step post-treatment procedures are necessary, which increase the complexity of mass production. Well-established CVD processes allow generation of MWCNTs, SWCNTs and graphene materials on a large scale. However, in order to achieve high electrochemical activities, surface functionalization of CNTs and graphene is usually an indispensable but expensive step in the device fabrication process. Generally, solution processes are relatively inexpensive, efficient and easy to scale up; the development of stable heterogeneous liquid mixtures consisting of nanocarbons and surface modifiers is beneficial for large-scale production of carbon-based electrochemical devices.

Moreover, slight variations in carbon structures can result in significant changes in electrochemical performance; therefore, careful and thorough microstructural characterization is always recommended to avoid potential misinterpretation of performance results. For example, single-layered, double-layered and multilayered graphene sheets have drastically different electronic properties and electrochemical capacitances; thus accurate determination of the number of graphene layers in an electrochemical device is important. Moreover, inadvertent adsorption of impurities significantly changes the electron transfer kinetics on carbon electrodes; detailed surface chemistry characterization is always necessary before drawing any conclusions on carbon microstructure-property relationships. Additionally, the roles of surface area and pore structure need to be considered when determining the correlation between electronic structures of carbon materials and their electrochemical activities.

1

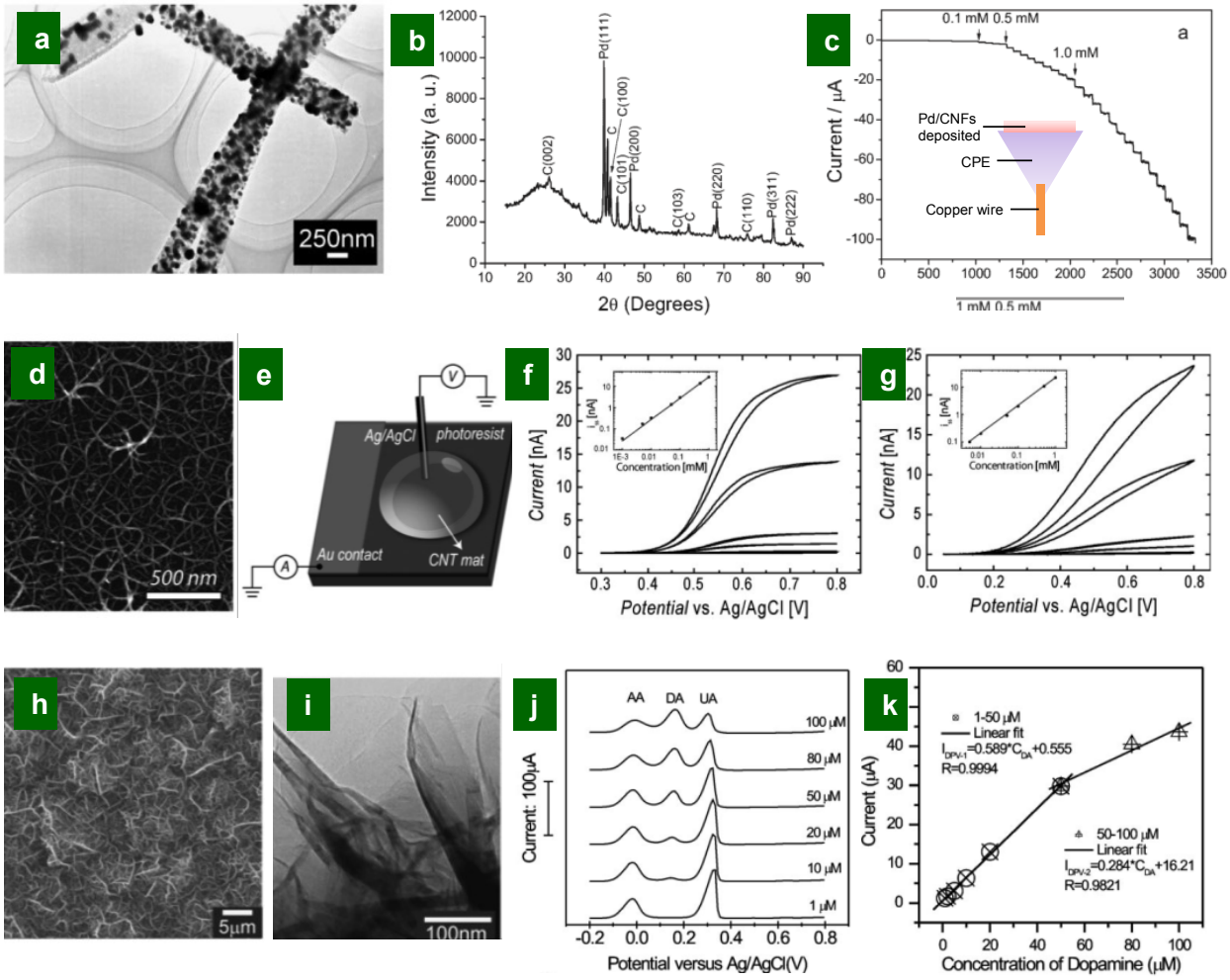

Figure 1. Carbon nanomaterials for electrochemical sensing. (a) TEM image of Pd/CNF nanocomposites. (b) XRD pattern of Pd/CNF nanocomposites. (c) Current-time response of the Pd/CNF-CPE on successive addition of H_2O_2 into N_2-saturated PBS; inset shows schematic illustration of a Pd/CNF-CPE sensing device. (d) FE-SEM image of a CNT mat. (e) Schematic of the 100 μM CNT mat UME and the experimental droplet cell set-up. (f-g) CVs of dopamine (f) from 1 μM to 1 mM in PBS, and (g) from 5 μM to 1 mM in 4% w/w albumin in PBS; Insets show the plots of limiting current (at 0.7 V vs. Ag/AgCl) versus dopamine concentration and the linear fits. (h) SEM image of MGNFs. (i) TEM image of MGNFs. (j) DPVs of the MGNF electrode in 50 mM PBS with 1 mM AA, 0.1 mM UA, and different concentrations of DA. (k) Peak current of DPV versus the DA concentration. Fig 1a-1c: reprinted with permission from ref [64]. Fig 1d-1g: reprinted with permission from ref [77]. Fig 1h-1k: reprinted with permission from ref [78].

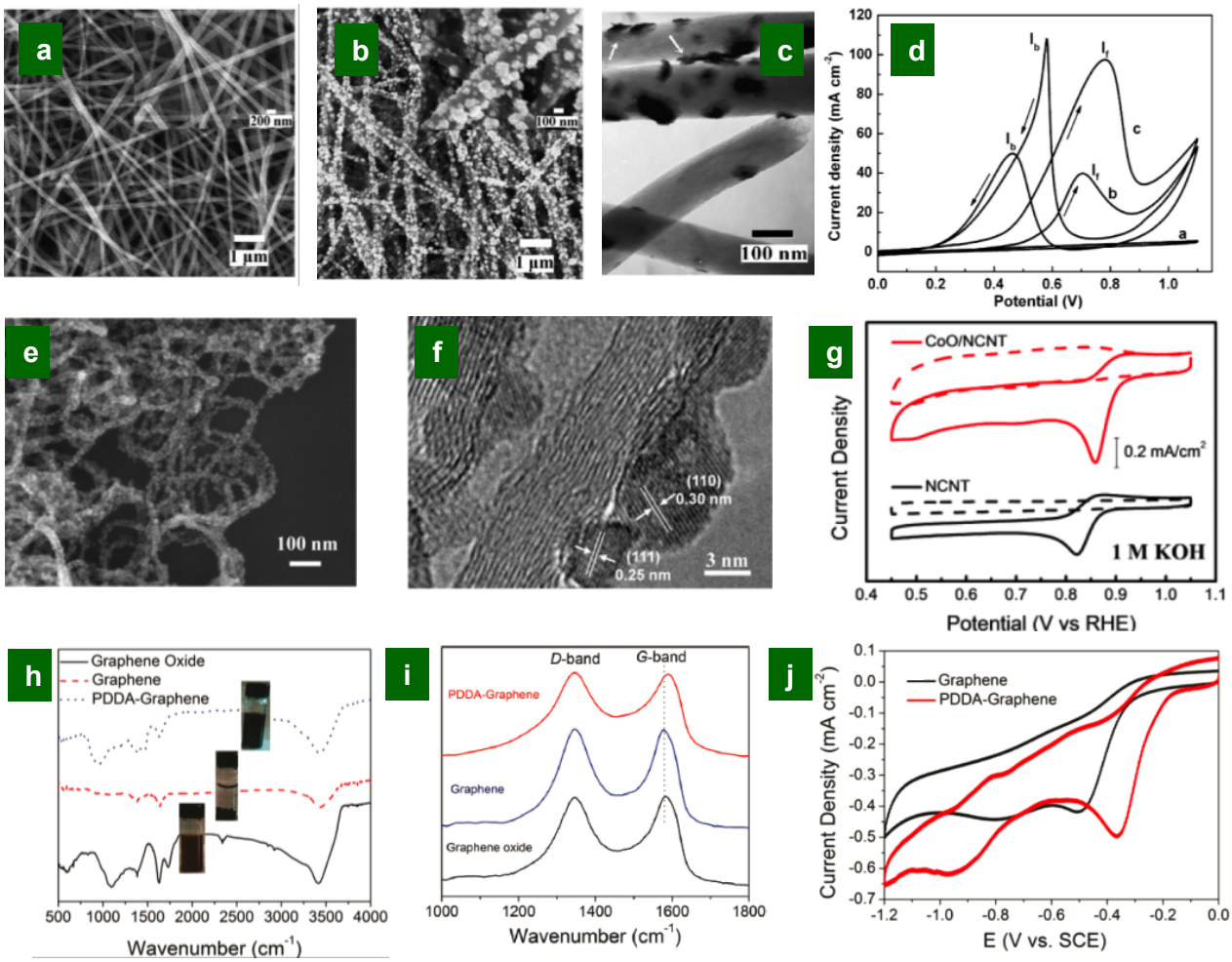

Figure 2. Carbon nanomaterials for electrocatalysis. (a,b) SEM images of (a) CNFs and (b) Pt/CNFs. (c) TEM image of Pt/CNFs. (d) CVs for methanol oxidation: a) CNF, b) Pt/C, and c) Pt/CNF. (e) SEM image of the CoO/NCNT hybrid. (f) TEM image of the CoO/NCNT hybrid. (g) CVs of CoO/NCNT and NCNT on glassy carbon electrodes in O_2-saturated (solid line) and N_2-saturated (dashed line) 1 M KOH. (h,i) (h) FTIR and (i) Raman spectra of graphene oxide, graphene, and PDDA-graphene. (j) CVs of oxygen reduction on the graphene and PDDA-graphene electrode in O_2-saturated 0.1 M KOH. Fig 2a-2d: reprinted with permission from ref [113]. Fig 2e-2g: reprinted with permission from ref [130]. Fig 2h-2j: reprinted with permission from ref [141].

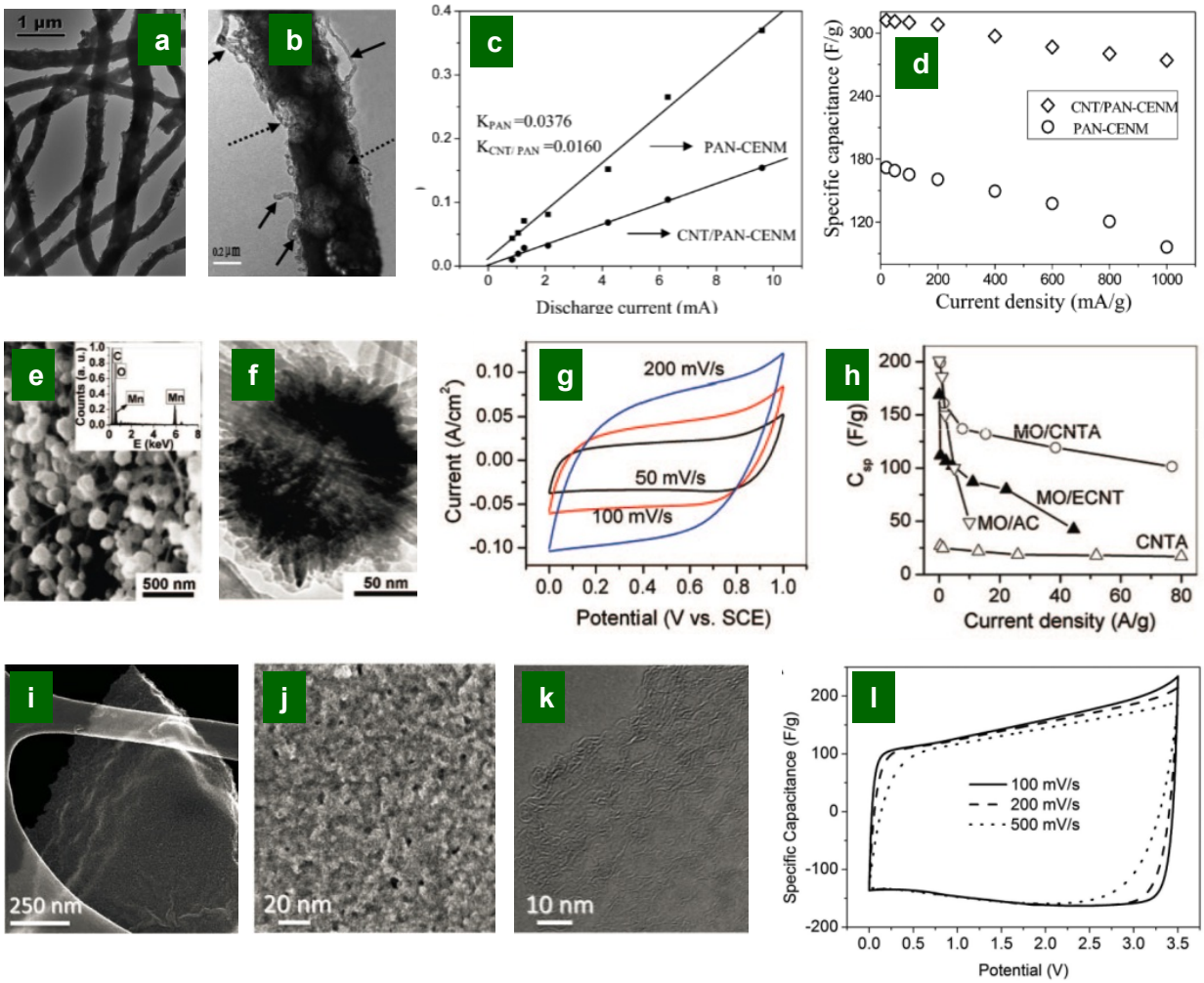

Figure 3. Carbon nanomaterials for supercapacitor applications. (a, b) SEM images of CNT-embedded carbonized electrospun nanofibers . The solid arrows in (b) indicate the CNTs exposed and the dashed arrows mark the large pores in the fiber. (c) Variation of the IR drop with discharge current for PAN-CENM and CNT/ PAN-CENM. (d) Specific capacitance versus current density for PAN-CENM and CNT/ PAN-CENM. (e) SEM image of the manganese oxide/CNTA composite and its EDX pattern (inset). (f) TEM image of a manganese oxide nanoflower. (g) CVs of the manganese oxide/CNTA composite. (h) Specific capacitance of manganese oxide/CNTA, manganese oxide/ECNT, manganese oxide/AC, and original CNTA versus discharge current density. (i) SEM image of a 3D a-MEGO piece. (j) High-resolution SEM image of a different sample region that demonstrates the porous morphology. (k) High-resolution phase contrast electron micrograph of the thin edge of an a-MEGO chunk, taken at 80 kV. (l) CVs of an a-MEGO based supercapacitor. Fig 3a-3d: reprinted with permission from ref [151]. Fig 3e-3h: reprinted with permission from ref [159]. Fig 3i-3l: reprinted with permission from ref [5].

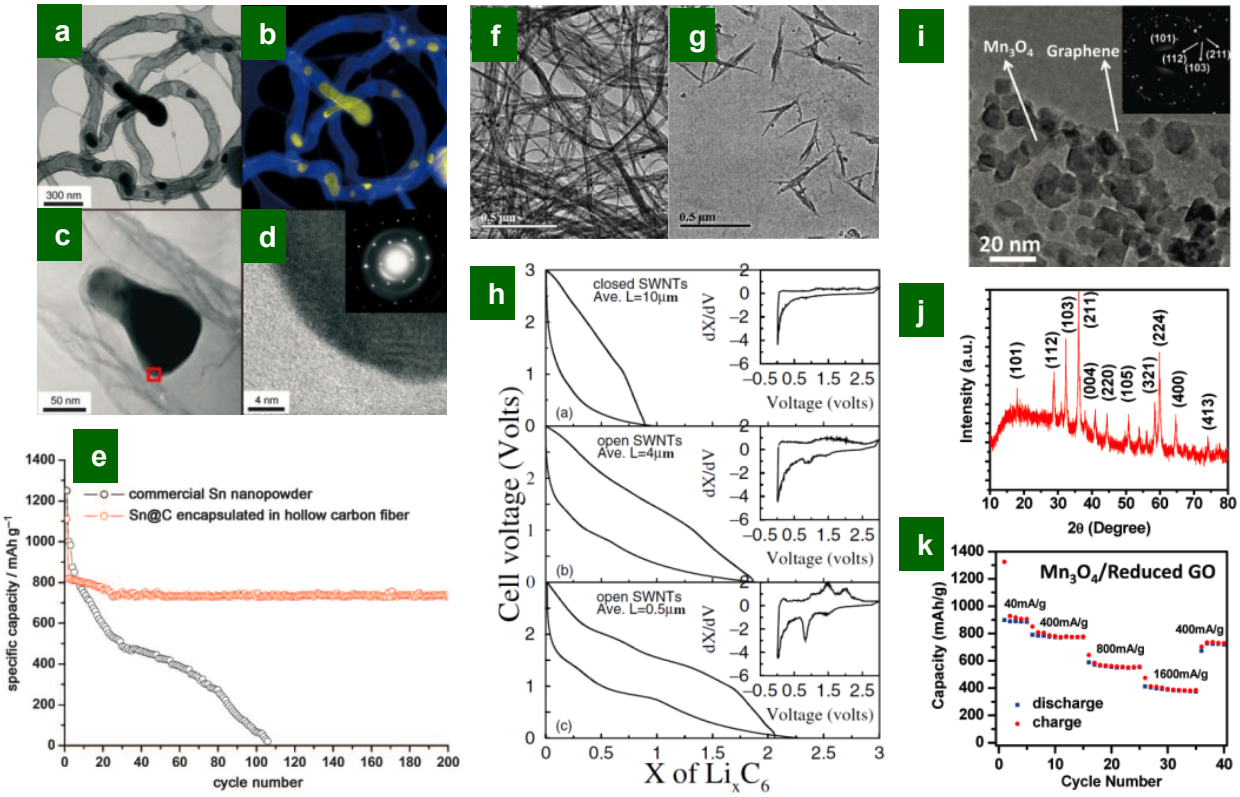

Figure 4. Carbon nanomaterials for LIB applications. (a) TEM image and (b) elemental mapping (carbon: blue; tin: yellow) of the CNFs containg Sn@C nanoparticles. (c) TEM image of an isolated Sn@C nanoparticle encapsulated in a hollow CNF. (d) HRTEM and SAED (inset) images of the region marked in (c) indicate the presence of single-crystalline metallic tin and graphitic carbon. (e) Capacity-cycle number curves of a Sn/C composite electrode and a commercial Sn nanopowder electrode at a cycling rate of 0.5 C. (f) TEM image of as-purified SWCNTs. (g) TEM image of SWCNTs after chemically etched for 24 h. (h) Second cycle intercalation and de-intercalation data: a) as purified SWCNTs, b) etched SWCNTs with an average bundle length of 4 μm, and c) etched SWCNTs with an average bundle length of 0.3 – 0.5 μm. (i) TEM image of Mn_3O_4/RGO; inset shows the electron diffraction pattern of the Mn_3O_4 nanoparticles on RGO. (j) XRD pattern of a packed thick film of Mn_3O_4/RGO. (k) Capacity retention of Mn_3O_4/RGO at various current densities. Fig 4a-4e: reprinted with permission from ref [184]. Fig 4f-4h: reprinted with permission from ref [195]. Fig 4i-4k: reprinted with permission from ref [207].

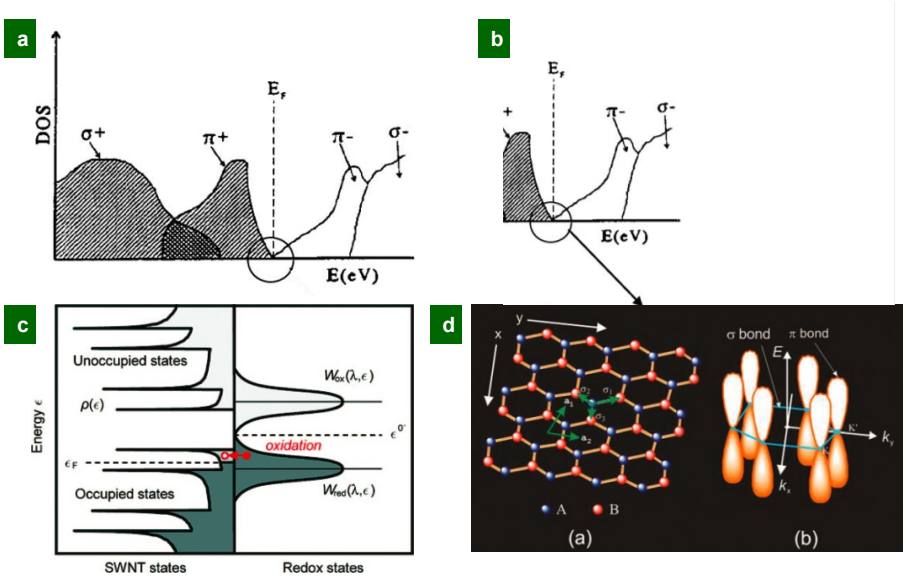

Figure 5. Electronic structure of carbon nanomaterials. (a) Calculated DOS of ideal single-crystal graphite. (b) Enlarged area of the circled region in (a). (c) Calculated DOS of a semiconducting SWCNT. (d) Electronic structure of a single-layer graphene. Fig 5a and 5b: reprinted with permission from ref [221]. Fig 5c: reprinted with permission from ref [222]. Fig 5d: reprinted with permission from ref [224].

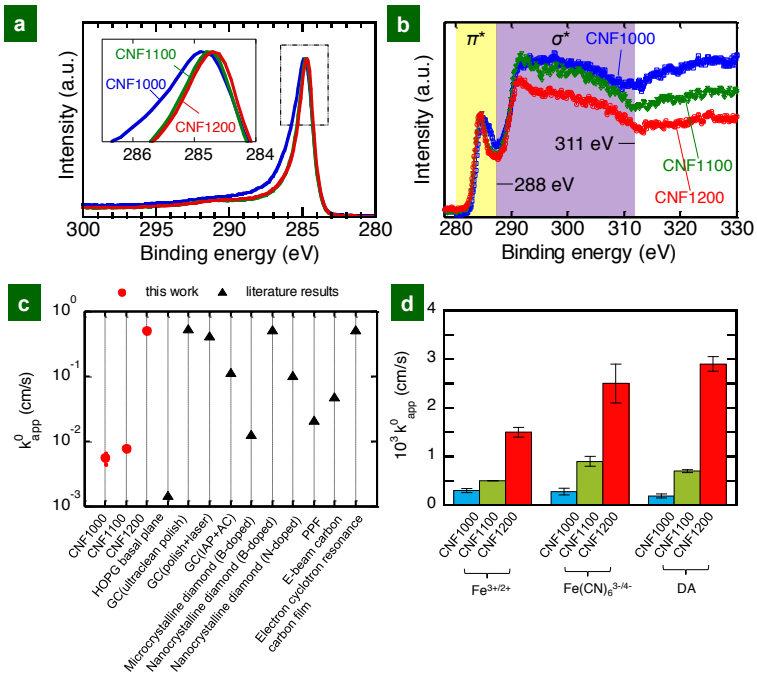

Figure 6. (a) XPS C 1s and (b) EELS spectra of CNF1000, CNF1100 and CNF1200. (c) Comparison of the apparent electron transfer rates k^0_{app} with literature results for $Ru(NH_3)_6^{3+/2+}$. (d) k^0_{app} for $Fe^{3+/2+}$, DA, and $Fe(CN)_6^{3-/4-}$. Reprinted with permission from ref [3].

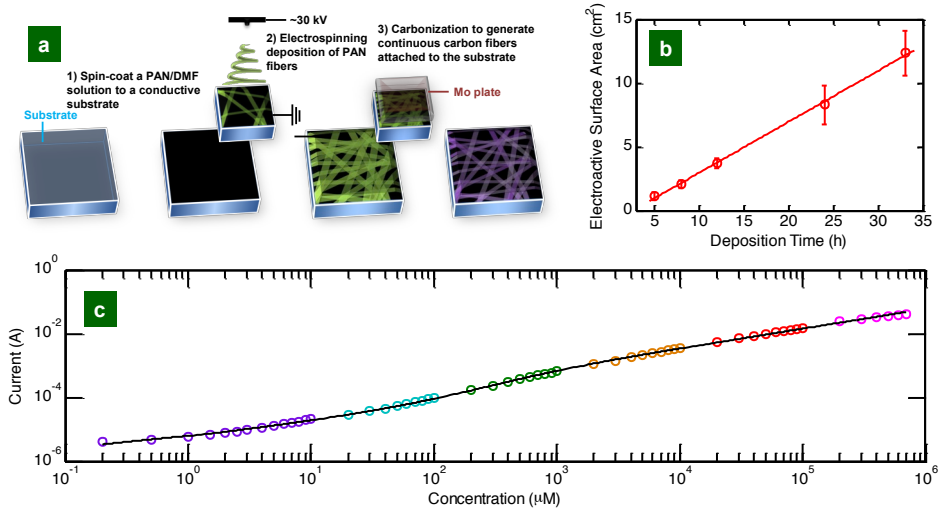

Figure 7. (a) Schematic illustration of the sensor fabrication process. (b) Calculated ESAs as a function of electrospinning deposition time. (c) Continuous nonlinear calibration curve for detection of dopamine with a concentration ranging from 0.2 to 700,000 μM. Reprinted with permission from ref [67].

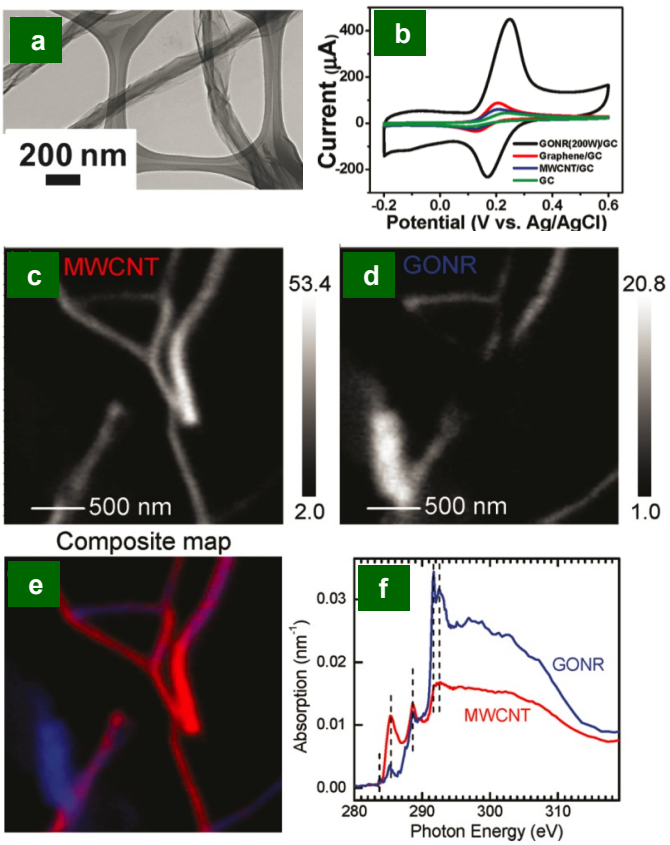

Figure 8. (a) TEM image of a MWCNT/GONR heterostructure. (b) CVs of MWCNT/GONR-, MWCNT-, and graphene-modified GC electrodes and the bare GC electrode in 1 mM DA. (c) – (e) Quantitative chemical mapping of the MWCNT/GONR structure: (c) MWCNT, (d) GONR, (e) color composite map with MWCNTs (red) and GONRs (blue). (f) C K-edge XANES of GONRs and MWCNTs from each pure region in (e). Reprinted with permission from ref [229].

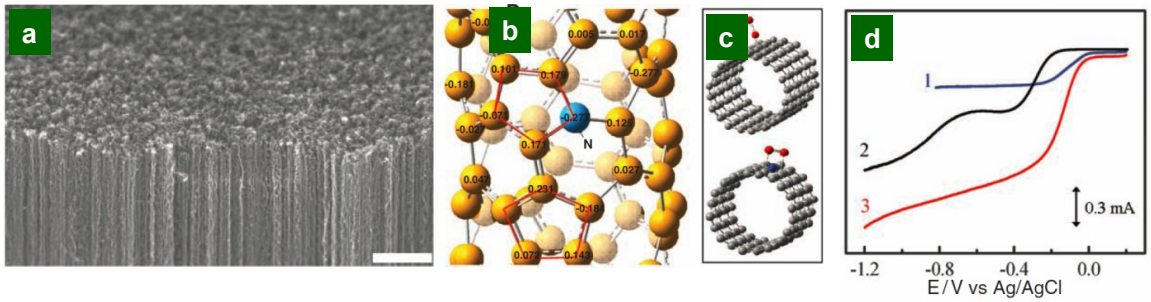

Figure 9. (a) SEM image of as-synthesized vertically aligned NCNTs prepared by pyrolysis of iron phthalocyannine (FePc) on a quartz substrate. Scale bar: 2 μm. (b) Calculated charge density distribution for the NCNTs. (c) Schematic representations of possible adsorption modes of an oxygen molecule at the CCNTs (top) and the NCNTs (bottom). (d) The steady-state voltammograms for oxygen reduction in air saturated 0.1 M KOH at the Pt-C (curve 1), VA-CCNT (curve 2), and VA-NCNT (curve 3) electrodes. Reprinted with permission from ref [132].

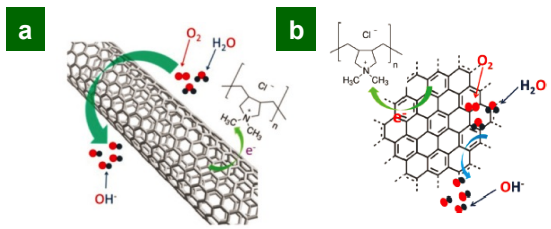

Figure 10. Illustration of the charge transfer process and oxygen reduction reaction on (a) PDDA-CNT and (b) PDDA-graphene. Reprinted with permission from ref [137, 141].

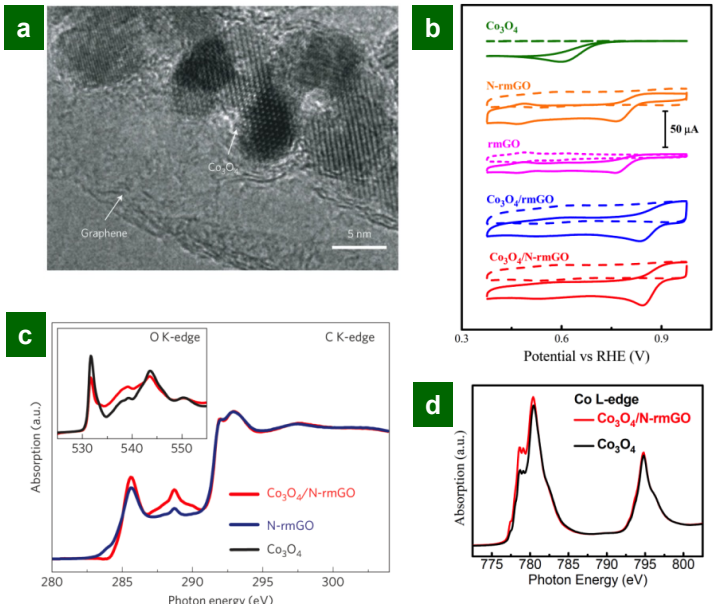

Figure 11. (a) TEM image of the Co_3O_4/N-rmGO hybrid. (b) CVs of Co_3O_4 nanocrystal, rmGO, N-rmGO, Co_3O_4/rmGO, and Co_3O_4/N-rmGO (all loaded on glassy carbon electrode with the same mass loading) in oxygen (solid) or argon (dash) saturated 0.1 M KOH. (c) C K-edge XANES of N-rmGO (blue curve) and Co_3O_4/N-rmGO (red curve). Inset shows O K-edge XANES of Co_3O_4 (black curve) and Co_3O_4/N-rmGO (red curve). (d) Co L-edge XANES of Co_3O_4 (black curve) and Co_3O_4/N-rmGO (red curve). The increase in the normalized peak area in the hybrid compared to Co_3O_4 indicates the increase of unoccupied Co 3d projected state in the hybrid, suggesting a lower electron density of the Co site in the hybrid. Reproduced with permission from ref [140].

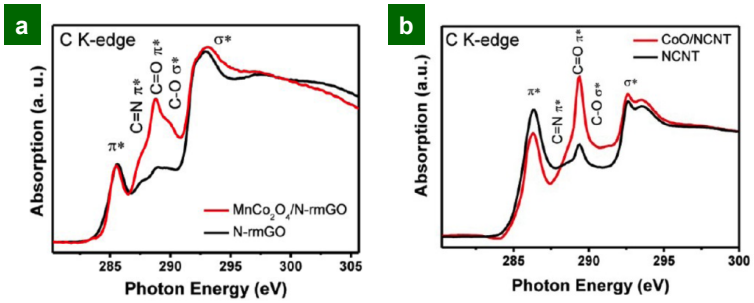

Figure 12. (a) C K-edge XANES of the $MnCo_2O_4$/N-rmGO hybrid and N-rmGO. Reproduced with permission from ref [129]. Copyright 2012 American Chemical Society. (b) C K-edge XANES of the CoO/N-CNT hybrid and N-CNT. Reproduced with permission from ref [130].

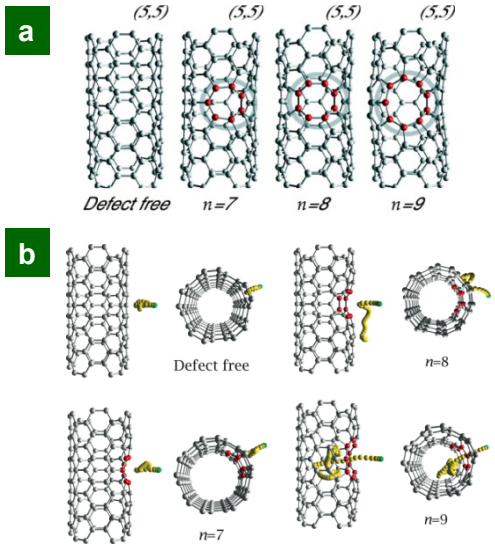

Figure 13. (a) Types of topological defects (rings of the red dots) in a (5,5) SWCNT. Here n = 7, 8, 9 means 7, 8, 9 carbon ring defects, respectively. (b) Effect of defects on Li insertion in a (5,5) SWCNT. Red balls indicate the defect, green balls indicate the initial position of the Li, and yellow balls indicate the trajectory of Li. For each nanotube, both the side view and the top view are shown. Reproduced with permission from ref [254].

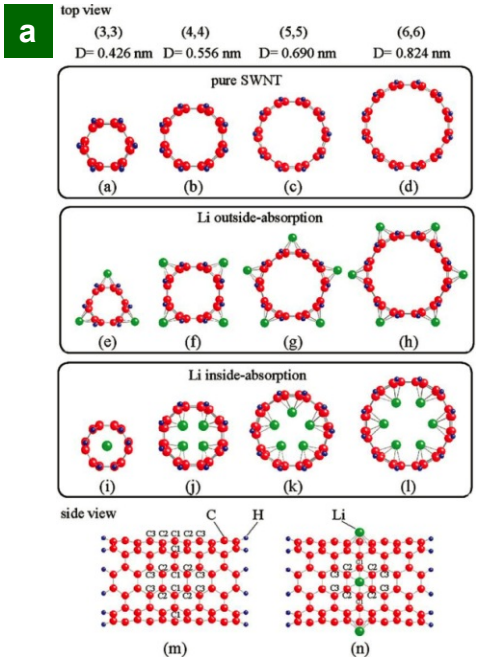

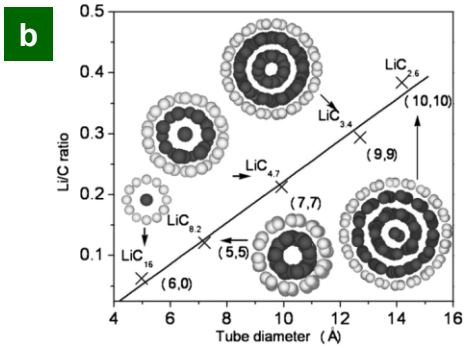

Figure 14. (a) a) $C_{66}H_{12}$; b) $C_{88}H_{16}$; c) $C_{110}H_{20}$; and d) $C_{132}H_{24}$ cluster models used for the calculations of the pure (3,3), (4,4), (5,5), and (6,6) SWCNTs; e) $Li_3C_{66}H_{12}$; f) $Li_4C_{88}H_{16}$; g) $Li_5C_{110}H_{20}$; and h) $Li_6C_{132}H_{24}$ cluster models used for the calculations of the Li outside absorption; i) $Li_3C_{66}H_{12}$; j) $Li_4C_{88}H_{16}$; k) $Li_5C_{110}H_{20}$; and l) $Li_6C_{132}H_{24}$ cluster models used for the calculations of the Li inside absorption. The figure a) to l) are top views from the mouth of nanotubes. The figures m and n are side views of the pure and Li outside-absorbed (6,6) nanotubes. Three kinds of carbon atoms, denoted by C_1, C_2 and C_3, are given in figures. Reproduced with permission from ref [231]. (b) The variation of Li/C ratio as a function of the tube diameter. The equilibrium configurations of SWCNTs filled with Li atoms are shown in the insets. White and gray balls represent C and Li atoms, respectively. Reproduced with permission from ref [232].

Table 1. Examples of Carbon Modification Methods for Electrochemical Applications in Sensing, Electrocatalysis, and Energy Storage.

	Electrospun CNFs	*References*	*CNTs/Graphene*	*References*
Electrochemical sensor	· Incorporation of metal nanoparticles · Manipulation of thermal treatment conditions	· [64-66] · [3, 261]	· Functionalization with conducting polymers · Modification with ion selective polyelectrolytes · Modification with metal oxides · Incorporation of enzymes · Doping with heteroatoms	· [79-81] · [82-84] · [85] · [84, 89] · [91, 92]
Electrocatalysts	· Incorporation of metal catalysts · Doping with heteroatoms · Pre-functionalization of CNFs	· [112-114, 116-119] · [111] · [115]	· Manipulation of surface chemistry · Use as supports to load metal catalysts · Doping with heteroatoms for metal-free electrocatalysis · Functionalization by electron-withdrawing polyelectrolytes · Functionalization by inorganic nanoparticles via strong chemical coupling	· [126-128] · [120-125] · [132, 139] · [138, 141] · [129, 130]
Supercapacitors	· Control of heat treatment conditions · Use of catalysts during carbonization and/or activation · Selection and combination of different polymer precursors · Incorporation of redox-active species · Encapsulation of highly conductive components	· [143] · [144, 145] · [146-148] · [149] · [150-152]	· Random entanglements of CNTs to produce mats · Vertical alignment of CNTs to improve rate performance · Modification with redox active polymers · Modification with metal oxides	· [153] · [159] · [17, 162] · [162, 159]
Lithium ion batteries	· Manipulation of carbonization conditions · Incorporation of Si · Incorporation of Sn · Incorporation of other electrochemically active metallic particles such as Co, Fe, Mn, Ni, and Cu	· [177] · [178, 179, 181-183] · [184, 185, 263-265] · [186-190]	· Opening or cutting of CNTs · Alignment of CNTs · Use as conductive additives for various cathode material systems · Creation of hybrids with metal oxides · Incorporation of chemical dopants · Control of layer structures	· [194] · [197-199] · [200-202] · [204-206] · [210] · [213]

References

[1] R. L. McCreery, *Chem Rev* **2008**, *108*, 2646.
[2] Y. P. Zhai, Y. Q. Dou, D. Y. Zhao, P. F. Fulvio, R. T. Mayes, S. Dai, *Adv Mater* **2011**, *23*, 4828.
[3] X. W. Mao, F. Simeon, G. C. Rutledge, T. A. Hatton, *Adv Mater* **2013**, *25*, 1309.
[4] D. Y. Pan, S. Wang, B. Zhao, M. H. Wu, H. J. Zhang, Y. Wang, et al., *Chem Mater* **2009**, *21*, 3136.
[5] Y. W. Zhu, S. Murali, M. D. Stoller, K. J. Ganesh, W. W. Cai, P. J. Ferreira, et al., *Science* **2011**, *332*, 1537.
[6] B. Gigliotti, B. Sakizzie, D. S. Bethune, R. M. Shelby, J. N. Cha, *Nano Lett* **2006**, *6*, 159.
[7] G. Lu, P. Maragakis, E. Kaxiras, *Nano Lett* **2005**, *5*, 897.
[8] N. W. S. Kam, Z. A. Liu, H. J. Dai, *Angew Chem Int Edit* **2006**, *45*, 577.
[9] M. Zheng, E. D. Semke, *J Am Chem Soc* **2007**, *129*, 6084.
[10] V. Sgobba, G. M. A. Rahman, D. M. Guldi, N. Jux, S. Campidelli, M. Prato, *Adv Mater* **2006**, *18*, 2264.
[11] C. Ehli, G. M. A. Rahman, N. Jux, D. Balbinot, D. M. Guldi, F. Paolucci, et al., *J Am Chem Soc* **2006**, *128*, 11222.
[12] D. M. Guldi, G. M. A. Rahman, M. Prato, N. Jux, S. H. Qin, W. Ford, *Angew Chem Int Edit* **2005**, *44*, 2015.
[13] X. Peng, N. Komatsu, S. Bhattacharya, T. Shimawaki, S. Aonuma, T. Kimura, et al., *Nat Nanotechnol* **2007**, *2*, 361.
[14] F. Y. Cheng, S. Zhang, A. Adronov, L. Echegoyen, F. Diederich, *Chem-Eur J* **2006**, *12*, 6062.
[15] D. M. Guldi, H. Taieb, G. M. A. Rahman, N. Tagmatarchis, M. Prato, *Adv Mater* **2005**, *17*, 871.
[16] X. Mao, G. C. Rutledge, T. A. Hatton, *Langmuir : the ACS journal of surfaces and colloids* **2013**, *29*, 9626.
[17] X. Mao, F. Simeon, D. S. Achilleos, G. C. Rutledge, T. A. Hatton, *J Mater Chem A* **2013**, *1*, 13120.
[18] J. Pinson, F. Podvorica, *Chem Soc Rev* **2005**, *34*, 429.
[19] A. Adenier, M. M. Chehimi, I. Gallardo, J. Pinson, N. Vila, *Langmuir* **2004**, *20*, 8243.
[20] J. M. Buriak, *Angew Chem Int Edit* **2001**, *40*, 532.
[21] C. W. Tornoe, C. Christensen, M. Meldal, *J Org Chem* **2002**, *67*, 3057.
[22] Walker, P. L.; Radovic, L. R. Chemistry and Physics of Carbon; Dekker: New York.
[23] Kinoshita, K. Carbon, Electrochemical and Physicochemical Properties; John Wiley and Sons: New York, 1988.
[24] McCreery, R. L. In Electroanalytical Chemistry; Bard, A. J., Ed. Dekker, New York, 1991; Vol 17.
[25] R. Bacon, *J Appl Phys* **1960**, *31*, 283.
[26] N. Saito, K. Aoki, Y. Usui, M. Shimizu, K. Hara, N. Narita, et al., *Chem Soc Rev* **2011**, *40*, 3824.
[27] L. S. Singer, I. C. Lewis, *Carbon* **1978**, *16*, 417.
[28] H.O. Pierson Handbook of carbon, graphite, diamond and fullerenes. Noyes Publications, New Jersey (1993)
[29] M. Inagaki, Y. Yang, F. Y. Kang, *Adv Mater* **2012**, *24*, 2547.
[30] M. N. Shuakat, T. Lin, *J Nanosci Nanotechno* **2014**, *14*, 1389.
[31] S. A. Theron, E. Zussman, A. L. Yarin, *Polymer* **2004**, *45*, 2017.
[32] N. Bhardwaj, S. C. Kundu, *Biotechnol Adv* **2010**, *28*, 325.
[33] W. E. Teo, S. Ramakrishna, *Nanotechnology* **2006**, *17*, R89.
[34] Z. C. Sun, E. Zussman, A. L. Yarin, J. H. Wendorff, A. Greiner, *Adv Mater* **2003**, *15*, 1929.
[35] E. Zussman, A. L. Yarin, A. V. Bazilevsky, R. Avrahami, M. Feldman, *Adv Mater* **2006**, *18*, 348.
[36] J. T. McCann, D. Li, Y. N. Xia, *Journal of Materials Chemistry* **2005**, *15*, 735.

[37] Y. Zhao, X. Y. Cao, L. Jiang, *J Am Chem Soc* **2007**, *129*, 764.
[38] S. Iijima, T. Ichihashi, *Nature* **1993**, *363*, 603.
[39] A. Thess, R. Lee, P. Nikolaev, H. J. Dai, P. Petit, J. Robert, et al., *Science* **1996**, *273*, 483.
[40] D. S. Bethune, C. H. Kiang, M. S. Devries, G. Gorman, R. Savoy, J. Vazquez, et al., *Nature* **1993**, *363*, 605.
[41] W. Z. Li, S. S. Xie, L. X. Qian, B. H. Chang, B. S. Zou, W. Y. Zhou, et al., *Science* **1996**, *274*, 1701.
[42] K. Hata, D. N. Futaba, K. Mizuno, T. Namai, M. Yumura, S. Iijima, *Abstr Pap Am Chem S* **2005**, *229*, U967.
[43] R. Sen, A. Govindaraj, C. N. R. Rao, *Chem Mater* **1997**, *9*, 2078.
[44] P. Nikolaev, M. J. Bronikowski, R. K. Bradley, F. Rohmund, D. T. Colbert, K. A. Smith, et al., *Chem Phys Lett* **1999**, *313*, 91.
[45] K. S. Novoselov, A. K. Geim, S. V. Morozov, D. Jiang, Y. Zhang, S. V. Dubonos, et al., *Science* **2004**, *306*, 666.
[46] H. P. Boehm, A. Clauss, U. Hofmann, G. O. Fischer, *Z Naturforsch Pt B* **1962**, *B 17*, 150.
[47] I. Forbeaux, J. M. Themlin, J. M. Debever, *Phys Rev B* **1998**, *58*, 16396.
[48] X. K. Lu, M. F. Yu, H. Huang, R. S. Ruoff, *Nanotechnology* **1999**, *10*, 269.
[49] K. V. Emtsev, A. Bostwick, K. Horn, J. Jobst, G. L. Kellogg, L. Ley, et al., *Nat Mater* **2009**, *8*, 203.
[50] C. Oshima, A. Nagashima, *J Phys-Condens Mat* **1997**, *9*, 1.
[51] W. S. Hummers, R. E. Offeman, *J Am Chem Soc* **1958**, *80*, 1339.
[52] S. Stankovich, D. A. Dikin, R. D. Piner, K. A. Kohlhaas, A. Kleinhammes, Y. Jia, et al., *Carbon* **2007**, *45*, 1558.
[53] S. Stankovich, R. D. Piner, X. Q. Chen, N. Q. Wu, S. T. Nguyen, R. S. Ruoff, *Journal of Materials Chemistry* **2006**, *16*, 155.
[54] V. C. Tung, M. J. Allen, Y. Yang, R. B. Kaner, *Nat Nanotechnol* **2009**, *4*, 25.
[55] C. Gomez-Navarro, R. T. Weitz, A. M. Bittner, M. Scolari, A. Mews, M. Burghard, et al., *Nano Lett* **2007**, *7*, 3499.
[56] S. J. Guo, S. J. Dong, *Chem Soc Rev* **2011**, *40*, 2644.
[57] S. Park, R. S. Ruoff, *Nat Nanotechnol* **2009**, *4*, 217.
[58] Y. Hernandez, V. Nicolosi, M. Lotya, F. M. Blighe, Z. Y. Sun, S. De, et al., *Nat Nanotechnol* **2008**, *3*, 563.
[59] M. Lotya, Y. Hernandez, P. J. King, R. J. Smith, V. Nicolosi, L. S. Karlsson, et al., *J Am Chem Soc* **2009**, *131*, 3611.
[60] K. S. Kim, Y. Zhao, H. Jang, S. Y. Lee, J. M. Kim, K. S. Kim, et al., *Nature* **2009**, *457*, 706.
[61] M. Hofmann, D. Nezich, A. Reina, J. Kong, *Nano Lett* **2008**, *8*, 4122.
[62] X. S. Li, W. W. Cai, J. H. An, S. Kim, J. Nah, D. X. Yang, et al., *Science* **2009**, *324*, 1312.
[63] A. Srivastava, C. Galande, L. Ci, L. Song, C. Rai, D. Jariwala, et al., *Chem Mater* **2010**, *22*, 3457.
[64] J. S. Huang, D. W. Wang, H. Q. Hou, T. Y. You, *Adv Funct Mater* **2008**, *18*, 441.
[65] Y. Liu, D. W. Wang, L. Xu, H. Q. Hou, T. Y. You, *Biosens Bioelectron* **2011**, *26*, 4585.
[66] G. Z. Hu, Z. P. Zhou, Y. Guo, H. Q. Hou, S. J. Shao, *Electrochem Commun* **2010**, *12*, 422.
[67] X. W. Mao, X. Q. Yang, G. C. Rutledge, T. A. Hatton, *Acs Appl Mater Inter* **2014**, *6*, 3394.
[68] C. Leger, P. Bertrand, *Chem Rev* **2008**, *108*, 2379.
[69] L. Stoica, R. Ludwig, D. Haltrich, L. Gorton, *Anal Chem* **2006**, *78*, 393.
[70] M. Pita, E. Katz, *J Am Chem Soc* **2008**, *130*, 36.
[71] K. A. Vincent, X. Li, C. F. Blanford, N. A. Belsey, J. H. Weiner, F. A. Armstrong, *Nat Chem Biol* **2007**, *3*, 760.
[72] J. A. Cracknell, K. A. Vincent, F. A. Armstrong, *Chem Rev* **2008**, *108*, 2439.
[73] S. C. Barton, J. Gallaway, P. Atanassov, *Chem Rev* **2004**, *104*, 4867.

[74] M. Hambourger, M. Gervaldo, D. Svedruzic, P. W. King, D. Gust, M. Ghirardi, et al., *J Am Chem Soc* **2008**, *130*, 2015.
[75] M. Burghard, H. Klauk, K. Kern, *Adv Mater* **2009**, *21*, 2586.
[76] P. J. Britto, K. S. V. Santhanam, P. M. Ajayan, *Bioelectroch Bioener* **1996**, *41*, 121.
[77] I. Dumitrescu, J. P. Edgeworth, P. R. Unwin, J. V. Macpherson, *Adv Mater* **2009**, *21*, 3105.
[78] N. G. Shang, P. Papakonstantinou, M. McMullan, M. Chu, A. Stamboulis, A. Potenza, et al., *Adv Funct Mater* **2008**, *18*, 3506.
[79] C. C. Hsueh, A. Brajtertoth, *Anal Chem* **1994**, *66*, 2458.
[80] Y. X. Li, P. Wang, L. Wang, X. Q. Lin, *Biosens Bioelectron* **2007**, *22*, 3120.
[81] J. X. Wen, L. Zhou, L. T. Jin, X. N. Cao, B. C. Ye, *J Chromatogr B* **2009**, *877*, 1793.
[82] D. Zheng, J. S. Ye, W. D. Zhang, *Electroanal* **2008**, *20*, 1811.
[83] S. Shahrokhian, H. R. Zare-Mehrjardi, *Electrochim Acta* **2007**, *52*, 6310.
[84] Y. C. Tsai, C. C. Chiu, *Sensor Actuat B-Chem* **2007**, *125*, 10.
[85] L. C. Jiang, W. D. Zhang, *Electroanal* **2009**, *21*, 1811.
[86] H. S. Han, J. M. You, H. Jeong, S. Jeon, *J Nanosci Nanotechno* **2014**, *14*, 4050.
[87] N. Butwong, L. Zhou, W. Ng-Eontae, R. Burakham, E. Moore, S. Srijaranai, et al., *J Electroanal Chem* **2014**, *717*, 41.
[88] W. Gao, W. W. Tjiu, J. C. Wei, T. X. Liu, *Talanta* **2014**, *120*, 484.
[89] L. Xiang, Y. Q. Lin, P. Yu, L. Su, L. Q. Mao, *Electrochim Acta* **2007**, *52*, 4144.
[90] M. B. Gholivand, M. Shamsipur, N. Amini, *Electrochim Acta* **2014**, *123*, 569.
[91] Q. H. Yang, W. H. Xu, A. Tomita, T. Kyotani, *J Am Chem Soc* **2005**, *127*, 8956.
[92] C. Y. Deng, J. H. Chen, M. D. Wang, C. H. Xiao, Z. Nie, S. Z. Yao, *Biosens Bioelectron* **2009**, *24*, 2091.
[93] S. Liu, Q. Shen, Y. Cao, L. Gan, Z. X. Wang, M. L. Steigerwald, et al., *Coordin Chem Rev* **2010**, *254*, 1101.
[94] H. B. Chu, L. Wei, R. L. Cui, J. Y. Wang, Y. Li, *Coordin Chem Rev* **2010**, *254*, 1117.
[95] C. E. Banks, R. G. Compton, *Analyst* **2005**, *130*, 1232.
[96] S. Alwarappan, A. Erdem, C. Liu, C. Z. Li, *J Phys Chem C* **2009**, *113*, 8853.
[97] L. P. Cai, R. Y. Zhan, K. Y. Pu, X. Y. Qi, H. Zhang, W. Huang, et al., *Anal Chem* **2011**, *83*, 7849.
[98] J. H. Jang, D. Rangappa, Y. U. Kwon, I. Honma, *Journal of Materials Chemistry* **2011**, *21*, 3462.
[99] X. Y. Zhang, L. L. Hou, A. Cnossen, A. C. Coleman, O. Ivashenko, P. Rudolf, et al., *Chem-Eur J* **2011**, *17*, 8957.
[100] S. Vadukumpully, J. Gupta, Y. P. Zhang, G. Q. Xu, S. Valiyaveettil, *Nanoscale* **2011**, *3*, 303.
[101] G. P. Keeley, N. McEvoy, H. Nolan, M. Holzinger, S. Cosnier, G. S. Duesberg, *Chem Mater* **2014**, *26*, 1807.
[102] J. J. Zhang, R. Y. Li, Z. J. Li, J. K. Liu, Z. G. Gu, G. L. Wang, *Nanoscale* **2014**, *6*, 5458.
[103] D. L. Jiang, Y. Zhang, H. Y. Chu, J. Liu, J. Wan, M. Chen, *Rsc Adv* **2014**, *4*, 16163.
[104] K. P. Prathish, M. M. Barsan, D. S. Geng, X. L. Sun, C. M. A. Brett, *Electrochim Acta* **2013**, *114*, 533.
[105] G. H. Yang, Y. H. Zhou, J. J. Wu, J. T. Cao, L. L. Li, H. Y. Liu, et al., *Rsc Adv* **2013**, *3*, 22597.
[106] Y. B. Zeng, Y. Zhou, L. Kong, T. S. Zhou, G. Y. Shi, *Biosens Bioelectron* **2013**, *45*, 25.
[107] Y. Zhang, X. P. Xiao, Y. J. Sun, Y. Shi, H. C. Dai, P. J. Ni, et al., *Electroanal* **2013**, *25*, 959.
[108] B. Q. Yuan, C. Y. Xu, D. H. Deng, Y. Xing, L. Liu, H. Pang, et al., *Electrochim Acta* **2013**, *88*, 708.
[109] H. Chen, M. B. Muller, K. J. Gilmore, G. G. Wallace, D. Li, *Adv Mater* **2008**, *20*, 3557.
[110] S. Koyama, Y. A. Kim, T. Hayashi, K. Takeuchi, C. Fujii, N. Kuroiwa, et al., *Carbon* **2009**, *47*, 1365.
[111] S. Maldonado, K. J. Stevenson, *J Phys Chem B* **2005**, *109*, 4707.
[112] M. Y. Li, S. Z. Zhao, G. Y. Han, B. S. Yang, *J Power Sources* **2009**, *191*, 351.

[113] M. Y. Li, G. Y. Han, B. S. Yang, *Electrochem Commun* **2008**, *10*, 880.
[114] X. M. Liu, M. Y. Li, G. Y. Han, J. H. Dong, *Electrochim Acta* **2010**, *55*, 2983.
[115] Z. Lin, L. W. Ji, W. E. Krause, X. W. Zhang, *J Power Sources* **2010**, *195*, 5520.
[116] Z. Lin, L. W. Ji, X. W. Zhang, *Electrochim Acta* **2009**, *54*, 7042.
[117] Z. Lin, L. W. Ji, O. Toprakci, W. Krause, X. W. Zhang, *J Mater Res* **2010**, *25*, 1329.
[118] J. S. Huang, H. Q. Hou, T. Y. You, *Electrochem Commun* **2009**, *11*, 1281.
[119] B. Jeong, S. Uhm, J. Lee, *Ecs Transactions* **2010**, *33*, 1757.
[120] T. Matsumoto, T. Komatsu, K. Arai, T. Yamazaki, M. Kijima, H. Shimizu, et al., *Chem Commun* **2004**, 840.
[121] W. Z. Li, C. H. Liang, J. S. Qiu, W. J. Zhou, H. M. Han, Z. B. Wei, et al., *Carbon* **2002**, *40*, 791.
[122] G. Girishkumar, K. Vinodgopal, P. V. Kamat, *J Phys Chem B* **2004**, *108*, 19960.
[123] H. Tang, J. H. Chen, S. Z. Yao, L. H. Nie, Y. F. Kuang, Z. P. Huang, et al., *Mater Chem Phys* **2005**, *92*, 548.
[124] B. Rajesh, K. R. Thampi, J. M. Bonard, N. Xanthopoulos, H. J. Mathieu, B. Viswanathan, *J Phys Chem B* **2003**, *107*, 2701.
[125] H. J. Ahn, W. J. Moon, T. Y. Seong, D. Wang, *Electrochem Commun* **2009**, *11*, 635.
[126] Y. Y. Shao, G. P. Yin, H. H. Wang, Y. Z. Gao, P. F. Shi, *J Power Sources* **2006**, *161*, 47.
[127] X. Wang, W. Z. Li, Z. W. Chen, M. Waje, Y. S. Yan, *J Power Sources* **2006**, *158*, 154.
[128] K. Prehn, R. Adelung, M. Heinen, S. P. Nunes, K. Schulte, *J Membrane Sci* **2008**, *321*, 123.
[129] Y. Y. Liang, H. L. Wang, J. G. Zhou, Y. G. Li, J. Wang, T. Regier, et al., *J Am Chem Soc* **2012**, *134*, 3517.
[130] Y. Y. Liang, H. L. Wang, P. Diao, W. Chang, G. S. Hong, Y. G. Li, et al., *J Am Chem Soc* **2012**, *134*, 15849.
[131] J. B. Yang, D. J. Liu, N. N. Kariuki, L. X. Chen, *Chem Commun* **2008**, 329.
[132] K. P. Gong, F. Du, Z. H. Xia, M. Durstock, L. M. Dai, *Science* **2009**, *323*, 760.
[133] R. Li, Z. D. Wei, X. L. Gou, W. Xu, *Rsc Adv* **2013**, *3*, 9978.
[134] S. B. Yang, L. J. Zhi, K. Tang, X. L. Feng, J. Maier, K. Mullen, *Adv Funct Mater* **2012**, *22*, 3634.
[135] S. Y. Wang, L. P. Zhang, Z. H. Xia, A. Roy, D. W. Chang, J. B. Baek, et al., *Angew Chem Int Edit* **2012**, *51*, 4209.
[136] J. Liang, Y. Jiao, M. Jaroniec, S. Z. Qiao, *Angew Chem Int Edit* **2012**, *51*, 11496.
[137] S. Y. Wang, D. S. Yu, L. M. Dai, *J Am Chem Soc* **2011**, *133*, 5182.
[138] L. T. Qu, Y. Liu, J. B. Baek, L. M. Dai, *Acs Nano* **2010**, *4*, 1321.
[139] P. P. Guo, F. Xiao, Q. Liu, H. F. Liu, Y. L. Guo, J. R. Gong, et al., *Sci Rep-Uk* **2013**, *3*.
[140] Y. Y. Liang, Y. G. Li, H. L. Wang, J. G. Zhou, J. Wang, T. Regier, et al., *Nat Mater* **2011**, *10*, 780.
[141] S. Y. Wang, D. S. Yu, L. M. Dai, D. W. Chang, J. B. Baek, *Acs Nano* **2011**, *5*, 6202.
[142] X. W. Mao, T. A. Hatton, G. C. Rutledge, *Curr Org Chem* **2013**, *17*, 1390.
[143] C. Kim, K. S. Yang, *Appl Phys Lett* **2003**, *83*, 1216.
[144] C. Kim, B. T. N. Ngoc, K. S. Yang, M. Kojima, Y. A. Kim, Y. J. Kim, et al., *Adv Mater* **2007**, *19*, 2341.
[145] J. S. Im, S. W. Woo, M. J. Jung, Y. S. Lee, *J Colloid Interface Sci* **2008**, *327*, 115.
[146] Y. W. Ju, S. H. Park, H. R. Jung, W. J. Lee, *J Electrochem Soc* **2009**, *156*, A489.
[147] H. T. Niu, J. Zhang, Z. L. Xie, X. G. Wang, T. Lin, *Carbon* **2011**, *49*, 2380.
[148] B. H. Kim, K. S. Yang, Y. A. Kim, Y. J. Kim, B. An, K. Oshida, *J Power Sources* **2011**, *196*, 10496.
[149] Y. W. Ju, G. R. Choi, H. R. Jung, C. Kim, K. S. Yang, W. J. Lee, *J Electrochem Soc* **2007**, *154*, A192.
[150] Y. W. Ju, G. R. Choi, H. R. Jung, W. J. Lee, *Electrochim Acta* **2008**, *53*, 5796.
[151] Q. H. Guo, X. P. Zhou, X. Y. Li, S. L. Chen, A. Seema, A. Greiner, et al., *Journal of Materials Chemistry* **2009**, *19*, 2810.

[152] S. J. Park, S. H. Im, *B Korean Chem Soc* **2008**, *29*, 777.
[153] C. M. Niu, E. K. Sichel, R. Hoch, D. Moy, H. Tennent, *Appl Phys Lett* **1997**, *70*, 1480.
[154] B. E. Conway, Electrochemical Supercapacitors: Scientific Fundamentals and Technological Applications, Kluwer Academic/Plenum, New York 1999
[155] K. H. An, W. S. Kim, Y. S. Park, J. M. Moon, D. J. Bae, S. C. Lim, et al., *Adv Funct Mater* **2001**, *11*, 387.
[156] A. Burke, M. Arulepp, Electrochem. Soc. Proc. 2001, 21, 576.
[157] G. Otrokhov, D. Pankratov, G. Shumakovich, M. Khlupova, Y. Zeifman, I. Vasil'eva, et al., *Electrochim Acta* **2014**, *123*, 151.
[158] P. X. Li, Y. B. Yang, E. Z. Shi, Q. C. Shen, Y. Y. Shang, S. T. Wu, et al., *Acs Appl Mater Inter* **2014**, *6*, 5228.
[159] H. Zhang, G. P. Cao, Z. Y. Wang, Y. S. Yang, Z. J. Shi, Z. N. Gu, *Nano Lett* **2008**, *8*, 2664.
[160] F. H. Su, M. H. Miao, *Nanotechnology* **2014**, *25*.
[161] K. Dai, C. H. Liang, J. M. Dai, L. H. Lu, G. P. Zhu, Z. L. Liu, et al., *Mater Chem Phys* **2014**, *143*, 1344.
[162] X. Zhao, B. M. Sanchez, P. J. Dobson, P. S. Grant, *Nanoscale* **2011**, *3*, 839.
[163] Y. C. Si, E. T. Samulski, *Chem Mater* **2008**, *20*, 6792.
[164] J. L. Xia, F. Chen, J. H. Li, N. J. Tao, *Nat Nanotechnol* **2009**, *4*, 505.
[165] M. D. Stoller, S. J. Park, Y. W. Zhu, J. H. An, R. S. Ruoff, *Nano Lett* **2008**, *8*, 3498.
[166] Y. W. Zhu, S. Murali, M. D. Stoller, A. Velamakanni, R. D. Piner, R. S. Ruoff, *Carbon* **2010**, *48*, 2118.
[167] Y. W. Zhu, M. D. Stoller, W. W. Cai, A. Velamakanni, R. D. Piner, D. Chen, et al., *Acs Nano* **2010**, *4*, 1227.
[168] Z. Tong, Y. Yang, J. Wang, J. Zhao, B. L. Su, Y. Li, *J Mater Chem A* **2014**, *2*, 4642.
[169] L. Wang, Y. J. Ye, X. P. Lu, Z. B. Wen, Z. Li, H. Q. Hou, et al., *Sci Rep-Uk* **2013**, *3*.
[170] S. H. Lee, H. W. Kim, J. O. Hwang, W. J. Lee, J. Kwon, C. W. Bielawski, et al., *Angew Chem Int Edit* **2010**, *49*, 10084.
[171] L. Sun, L. Wang, C. G. Tian, T. X. Tan, Y. Xie, K. Y. Shi, et al., *Rsc Adv* **2012**, *2*, 4498.
[172] Z. S. Wu, A. Winter, L. Chen, Y. Sun, A. Turchanin, X. L. Feng, et al., *Adv Mater* **2012**, *24*, 5130.
[173] Y. S. Yun, H. H. Park, H. J. Jin, *Materials* **2012**, *5*, 1258.
[174] Y. Zhao, C. G. Hu, Y. Hu, H. H. Cheng, G. Q. Shi, L. T. Qu, *Angew Chem Int Edit* **2012**, *51*, 11371.
[175] J. Han, L. L. Zhang, S. Lee, J. Oh, K. S. Lee, J. R. Potts, et al., *Acs Nano* **2013**, *7*, 19.
[176] E. Iyyamperumal, S. Y. Wang, L. M. Dai, *Acs Nano* **2012**, *6*, 5259.
[177] C. Kim, K. S. Yang, M. Kojima, K. Yoshida, Y. J. Kim, Y. A. Kim, et al., *Adv Funct Mater* **2006**, *16*, 2393.
[178] C. K. Chan, H. L. Peng, G. Liu, K. McIlwrath, X. F. Zhang, R. A. Huggins, et al., *Nat Nanotechnol* **2008**, *3*, 31.
[179] H. Kim, B. Han, J. Choo, J. Cho, *Angew Chem Int Edit* **2008**, *47*, 10151.
[180] X. W. Zhang, P. K. Patil, C. S. Wang, A. J. Appleby, F. E. Little, D. L. Cocke, *J Power Sources* **2004**, *125*, 206.
[181] L. W. Ji, A. J. Medford, X. W. Zhang, *Journal of Materials Chemistry* **2009**, *19*, 5593.
[182] L. W. Ji, X. W. Zhang, *Carbon* **2009**, *47*, 3219.
[183] L. W. Ji, X. W. Zhang, *Electrochem Commun* **2009**, *11*, 1146.
[184] Y. Yu, L. Gu, C. L. Wang, A. Dhanabalan, P. A. van Aken, J. Maier, *Angew Chem Int Edit* **2009**, *48*, 6485.
[185] Y. Yu, L. Gu, C. B. Zhu, P. A. van Aken, J. Maier, *J Am Chem Soc* **2009**, *131*, 15984.
[186] L. Wang, Y. Yu, P. C. Chen, C. H. Chen, *Scripta Mater* **2008**, *58*, 405.
[187] L. Wang, Y. Yu, P. C. Chen, D. W. Zhang, C. H. Chen, *J Power Sources* **2008**, *183*, 717.
[188] L. W. Ji, X. W. Zhang, *Electrochem Commun* **2009**, *11*, 795.

[189] L. W. Ji, Z. Lin, A. J. Medford, X. W. Zhang, *Chem-Eur J* **2009**, *15*, 10718.
[190] L. W. Ji, Z. Lin, R. Zhou, Q. Shi, O. Toprakci, A. J. Medford, et al., *Electrochim Acta* **2010**, *55*, 1605.
[191] B. Gao, A. Kleinhammes, X. P. Tang, C. Bower, L. Fleming, Y. Wu, et al., *Chem Phys Lett* **1999**, *307*, 153.
[192] A. S. Claye, J. E. Fischer, C. B. Huffman, A. G. Rinzler, R. E. Smalley, *J Electrochem Soc* **2000**, *147*, 2845.
[193] F. N. Almajhdi, H. Fouad, K. A. Khalil, H. M. Awad, S. H. S. Mohamed, T. Elsarnagawy, et al., *J Mater Sci-Mater M* **2014**, *25*, 1045.
[194] F. Leroux, K. Metenier, S. Gautier, E. Frackowiak, S. Bonnamy, F. Beguin, *J Power Sources* **1999**, *81*, 317.
[195] H. Shimoda, B. Gao, X. P. Tang, A. Kleinhammes, L. Fleming, Y. Wu, et al., *Phys Rev Lett* **2002**, *88*.
[196] W. H. Shin, H. M. Jeong, B. G. Kim, J. K. Kang, J. W. Choi, *Nano Lett* **2012**, *12*, 2283.
[197] G. X. Wang, J. Yao, H. K. Liu, S. X. Dou, J. H. Ahn, *Met Mater-Int* **2006**, *12*, 413.
[198] H. Zhang, G. P. Cao, Y. S. Yang, Z. N. Gu, *J Electrochem Soc* **2008**, *155*, K19.
[199] D. N. Futaba, K. Hata, T. Yamada, T. Hiraoka, Y. Hayamizu, Y. Kakudate, et al., *Nat Mater* **2006**, *5*, 987.
[200] J. Zhao, Q. Y. Gao, C. Gu, Y. Yang, *Chem Phys Lett* **2002**, *358*, 77.
[201] K. Sheem, Y. H. Lee, H. S. Lim, *J Power Sources* **2006**, *158*, 1425.
[202] L. Wang, Y. D. Huang, R. R. Jiang, D. Z. Jia, *J Electrochem Soc* **2007**, *154*, A1015.
[203] J. S. Sakamoto, B. Dunn, *J Electrochem Soc* **2002**, *149*, A26.
[204] M. H. Liang, L. J. Zhi, *Journal of Materials Chemistry* **2009**, *19*, 5871.
[205] D. H. Wang, D. W. Choi, J. Li, Z. G. Yang, Z. M. Nie, R. Kou, et al., *Acs Nano* **2009**, *3*, 907.
[206] D. H. Wang, R. Kou, D. Choi, Z. G. Yang, Z. M. Nie, J. Li, et al., *Acs Nano* **2010**, *4*, 1587.
[207] H. L. Wang, L. F. Cui, Y. A. Yang, H. S. Casalongue, J. T. Robinson, Y. Y. Liang, et al., *J Am Chem Soc* **2010**, *132*, 13978.
[208] L. Zhang, H. B. Wu, X. W. Lou, *Adv Energy Mater* **2014**, *4*.
[209] S. K. Park, A. Jin, S. H. Yu, J. Ha, B. Jang, S. Bong, et al., *Electrochim Acta* **2014**, *120*, 452.
[210] P. C. Lian, J. Y. Wang, D. D. Cai, L. X. Ding, Q. M. Jia, H. H. Wang, *Electrochim Acta* **2014**, *116*, 103.
[211] A. L. M. Reddy, A. Srivastava, S. R. Gowda, H. Gullapalli, M. Dubey, P. M. Ajayan, *Acs Nano* **2010**, *4*, 6337.
[212] Z. S. Wu, W. C. Ren, L. Xu, F. Li, H. M. Cheng, *Acs Nano* **2011**, *5*, 5463.
[213] W. J. Lee, T. H. Hwang, J. O. Hwang, H. W. Kim, J. Lim, H. Y. Jeong, et al., *Energ Environ Sci* **2014**, *7*, 621.
[214] E. Yoo, J. Kim, E. Hosono, H. Zhou, T. Kudo, I. Honma, *Nano Lett* **2008**, *8*, 2277.
[215] S. Petnikota, N. K. Rotte, V. V. S. S. Srikanth, B. S. R. Kota, M. V. Reddy, K. P. Loh, et al., *J Solid State Electr* **2014**, *18*, 941.
[216] H. B. Wang, C. J. Zhang, Z. H. Liu, L. Wang, P. X. Han, H. X. Xu, et al., *Journal of Materials Chemistry* **2011**, *21*, 5430.
[217] Z. L. Wang, D. Xu, H. G. Wang, Z. Wu, X. B. Zhang, *Acs Nano* **2013**, *7*, 2422.
[218] W. J. Royea, T. W. Hamann, B. S. Brunschwig, N. S. Lewis, *J Phys Chem B* **2006**, *110*, 19433.
[219] K. Kokko, E. Ojala, K. Mansikka, *Phys Status Solidi B* **1989**, *153*, 235.
[220] H. Gerischer, R. Mcintyre, D. Scherson, W. Storck, *J Phys Chem-Us* **1987**, *91*, 1930.
[221] M. S. Dresselhaus, G. Dresselhaus, J. E. Fischer, *Phys Rev B* **1977**, *15*, 3180.
[222] I. Heller, J. Kong, K. A. Williams, C. Dekker, S. G. Lemay, *J Am Chem Soc* **2006**, *128*, 7353.
[223] Bard, A. J.; Faulkner, L. R. Electrochemical Methods; 2nd ed.; Wiley: New York, 2001.
[224] D. Chen, L. H. Tang, J. H. Li, *Chem Soc Rev* **2010**, *39*, 3157.
[225] M. I. Katsnelson, K. S. Novoselov, A. K. Geim, *Nat Phys* **2006**, *2*, 620.
[226] Y. B. Zhang, Y. W. Tan, H. L. Stormer, P. Kim, *Nature* **2005**, *438*, 201.

[227] K. S. Novoselov, E. McCann, S. V. Morozov, V. I. Fal'ko, M. I. Katsnelson, U. Zeitler, et al., *Nat Phys* **2006**, *2*, 177.
[228] K. S. Novoselov, A. K. Geim, S. V. Morozov, D. Jiang, M. I. Katsnelson, I. V. Grigorieva, et al., *Nature* **2005**, *438*, 197.
[229] C. L. Sun, C. T. Chang, H. H. Lee, J. G. Zhou, J. Wang, T. K. Sham, et al., *Acs Nano* **2011**, *5*, 7788.
[230] U. N. Maiti, W. J. Lee, J. M. Lee, Y. Oh, J. Y. Kim, J. E. Kim, et al., *Adv Mater* **2014**, *26*, 40.
[231] Y. Liu, H. Yukawa, M. Morinaga, *Comp Mater Sci* **2004**, *30*, 50.
[232] M. W. Zhao, Y. Y. Xia, X. D. Liu, Z. Y. Tan, B. D. Huang, F. Li, et al., *Phys Lett A* **2005**, *340*, 434.
[233] K. J. Koivusaari, T. T. Rantala, S. Leppavuori, *Diam Relat Mater* **2000**, *9*, 736.
[234] S. Hrapovic, Y. L. Liu, K. B. Male, J. H. T. Luong, *Anal Chem* **2004**, *76*, 1083.
[235] X. H. Cao, L. X. Zhang, W. P. Cai, Y. Q. Li, *Electrochem Commun* **2010**, *12*, 540.
[236] K. Min, Y. J. Yoo, *Talanta* **2009**, *80*, 1007.
[237] U. Yogeswaran, S. M. Chen, *Sensor Actuat B-Chem* **2008**, *130*, 739.
[238] Y. Z. Zhang, Y. Pan, S. Sit, L. P. Zhang, S. P. Li, M. W. Shao, *Electroanal* **2007**, *19*, 1695.
[239] X. W. Kan, Y. Zhao, Z. R. Geng, Z. L. Wang, J. J. Zhu, *J Phys Chem C* **2008**, *112*, 4849.
[240] R. Manjunatha, G. S. Suresh, J. S. Melo, S. F. D'Souza, T. V. Venkatesha, *Sensor Actuat B-Chem* **2010**, *145*, 643.
[241] Z. A. Alothman, N. Bukhari, S. M. Wabaidur, S. Haider, *Sensor Actuat B-Chem* **2010**, *146*, 314.
[242] Y. R. Kim, S. Bong, Y. J. Kang, Y. Yang, R. K. Mahajan, J. S. Kim, et al., *Biosens Bioelectron* **2010**, *25*, 2366.
[243] S. Q. Liu, W. H. Sun, F. T. Hu, *Sensor Actuat B-Chem* **2012**, *173*, 497.
[244] X. Liu, L. L. Xie, H. L. Li, *J Electroanal Chem* **2012**, *682*, 158.
[245] Q. Liu, X. Zhu, Z. H. Huo, X. L. He, Y. Liang, M. T. Xu, *Talanta* **2012**, *97*, 557.
[246] D. X. Han, T. T. Han, C. S. Shan, A. Ivaska, L. Niu, *Electroanal* **2010**, *22*, 2001.
[247] Y. Zhang, R. Yuan, Y. Q. Chai, W. J. Li, X. Zhong, H. A. Zhong, *Biosens Bioelectron* **2011**, *26*, 3977.
[248] S. L. Yang, D. N. Wang, G. X. Liang, Y. M. Yiu, J. J. Wang, L. J. Liu, et al., *Energ Environ Sci* **2012**, *5*, 7007.
[249] Z. Shi, J. J. Zhang, Z. S. Liu, H. J. Wang, D. P. Wilkinson, *Electrochim Acta* **2006**, *51*, 1905.
[250] N. A. Kaskhedikar, J. Maier, *Adv Mater* **2009**, *21*, 2664.
[251] S. Kawasaki, T. Hara, Y. Iwai, Y. Suzuki, *Mater Lett* **2008**, *62*, 2917.
[252] A. Udomvech, T. Kepdcharoen, *J Korean Phys Soc* **2008**, *52*, 1350.
[253] W. X. Chen, J. Y. Lee, Z. L. Liu, *Carbon* **2003**, *41*, 959.
[254] K. Nishidate, M. Hasegawa, *Phys Rev B* **2005**, *71*.
[255] C. Garau, A. Frontera, D. Quinonero, A. Costa, P. Ballester, P. M. Deya, *Chem Phys Lett* **2003**, *374*, 548.
[256] C. Garau, A. Frontera, D. Quinonero, A. Costa, P. Ballester, P. M. Deya, *Chem Phys* **2004**, *297*, 85.
[257] V. Meunier, J. Kephart, C. Roland, J. Bernholc, *Phys Rev Lett* **2002**, *88*.
[258] G. X. Wang, X. P. Shen, J. Yao, J. Park, *Carbon* **2009**, *47*, 2049.
[259] R. Mukherjee, A. V. Thomas, A. Krishnamurthy, N. Koratkar, *Acs Nano* **2012**, *6*, 7867.
[260] C. C. Ma, X. H. Shao, D. P. Cao, *Journal of Materials Chemistry* **2012**, *22*, 8911.
[261] Y. F. Li, Z. Zhou, L. B. Wang, *J Chem Phys* **2008**, *129*.
[262] K. M. Forward, A. Flores, G. C. Rutledge, *Chem Eng Sci* **2013**, *104*, 250.